Scanning Microscopy

Volume 3 | Number 4 Article 9

11-27-1989

Analytical Description of X-Ray Peaks: Application to L X-Ray Spectra Processing of Lanthanide Elements by Means of the Electron Probe Micro-Analyzer

G. Remond
Bureau de Recherches Géologiques et Minières

Ph. Coutures
Bureau de Recherches Géologiques et Minières

C. Gilles
Bureau de Recherches Géologiques et Minières

D. Massiot
CNRS

Scanning Microscopy, Vol. 3, No. 4, 1989 (Pages 1059-1086) 0891-7035/89$3.00+.00
Scanning Microscopy International, Chicago (AMF O'Hare), IL 60666 USA

ANALYTICAL DESCRIPTION OF X-RAY PEAKS : APPLICATION TO L X-RAY SPECTRA PROCESSING OF LANTHANIDE ELEMENTS BY MEANS OF THE ELECTRON PROBE MICRO-ANALYZER

G. REMOND(1)*, Ph. COUTURES(1), C. GILLES(1), D. MASSIOT(2).

(1) Bureau de Recherches Géologiques et Minières, ORLEANS, FRANCE
(2) CNRS, Centre de Recherches sur la Physique des Hautes Températures, ORLEANS, FRANCE

(Received for publication March 30, 1989, and in revised form November 27, 1989)

Abstract

The shape of Lα X-ray peaks analyzed by means of a LiF (200 plane) monochromator was described by a pseudo-Voigt function :

$$P(\lambda) = 0.35\ P_1(\lambda) + 0.65\ P_2(\lambda)$$

where $P_1(\lambda)$ and $P_2(\lambda)$ are a Gaussian and a Lorentzian distribution centered at the same wavelength, with the same amplitude and half-width and in relative proportion 0.35 and 0.65 respectively. For peaks occurring at wavelength greater than ≃ 0.17 nm, a Gaussian offset was added in order to correct the asymmetry of peaks resulting from the monochromator mounting within the spectrometer.

The effective wavelength resolution was obtained by quadrature addition of the instrumental resolution and the natural width of the X-ray peaks. It has been shown that the difference in peak width of the L emission peaks of the lanthanide elements resulted from their difference in their natural widths. For these elements, the $L\beta_2$, $L\gamma_1$ and $L\gamma_2$ were found to be accompanied by non-diagram lines, $L\beta_{14}$, $L\gamma_9$ and $L\gamma_{10}$ respectively. The wavelength separation distances $L\beta_{14}$-$L\beta_2$, $L\gamma_9$-$L\gamma_1$ and $L\gamma_{10}$-$L\gamma_2$ were found consistent with the distances derived from the plasmon theory.

Key words : Wavelength dispersive spectrometry, peak shape, resolution, natural width, non-diagram lines, lanthanide elements, electron probe microanalysis.

* Address for correspondence :

G. REMOND - B.R.G.M - Departement Analyse - BP 6009 - 45060 ORLEANS CEDEX 2 (FRANCE)

Phone n° (33) 38 64 31 23

Introduction

Besides petrological applications, it is now of growing interest to have accurate chemical analyses of rare-earth element bearing minerals in order to improve the recovery of these elements which are involved in technological compounds such as lasers, magnets, glasses, ceramics. Because present analytical methods (e.g., wet chemistry, neutron activation) lead to average composition and are generally destructive, it is essential to provide non-destructive point analytical techniques.

Only rare-earth elements belonging to the lantanide element series ($57 \leq Z \leq 71$) will be considered in the present study. Quantitative X-ray analysis of lanthanide elements bearing compounds has been reported for both wavelength dispersive spectrometry (WDS) (18) and energy dispersive spectrometry (EDS) (25) by means of the electron probe microanalyzer (EPMA). These elements are usually analyzed with the EPMA by means of L spectra for which at least ten lines are detectable for each element. In addition, within natural compounds or technological materials it is common for high concentrations of some lanthanide elements to be associated with low concentrations of the others. Thus, X-ray spectra of these compounds are complex leading to common peak interferences, and accurate measurement of the intensities is difficult.

To obtain intensity data free of interferences, a common approach is to apply predetermined "overlap coefficients" to the raw intensities (18),(25). By the use of a computer controlled EPMA an alternative approach to remove the continuum background and overlapping peaks consists of processing

digitally recorded WDS spectra using digital filtering and least-squares peak fitting as usually done in EDS data processing (15).

Accurate relative intensities of X-ray peaks for each lanthanide element must be known in order to process complex L X-ray spectra (13). The relative intensity of the peaks with respect to the Lα line intensity given in the literature (6) are generally considered to be the same for all the lanthanide elements (e.g., $L\beta_1$ = 50, $L\beta_2$ = 20, $L\beta_3$ = 6). The X-ray intensity ratio I Kβ/I Kα has been extensively studied but the prediction of the relative transition probabilities involved in L X-ray emissions is much more complex owing to the probability of non-radiative transitions (Coster Kronig transitions) which are equivalent to an Auger emission mechanism occurring between the L levels. In addition, the relative intensities of L lines may be modified by the existence of non-diagram or satellite lines whose energies cannot be expressed as the difference of two levels in the energy-level diagram. These satellite lines have weak intensities and may occur either on the high or low energy side of the major peak (8).

The lanthanide elements have partially filled 4f shells resulting in an electronic configuration similar to that existing for the transition elements ($21 \leq Z \leq 29$), where the 3d shells are partially filled. Asymmetry of K X-ray spectra of the transition elements has been reported (20) (28), (30) (31) and associated with non-diagram lines (satellite lines) occurring on the low energy side of the major monoenergetic peak. The theories of satellite lines have been reviewed by Edwards (8). Similar satellite lines are expected to accompany X-ray radiative transitions originating from the incompletely filled 4f levels of the lanthanide elements (2) (19) (23) (29). The satellite lines leading to departure from symmetry of peaks have been shown to be much stronger than those accompanying the K spectra of the transition elements.

Accurate interpretation of complex L X-ray spectra including non-diagram lines characteristic of the specific electronic configuration of the analyzed lanthanide element, requires an accurate analytical description of the line shape of each X-ray peak recorded by the spectrometer.

This analytical description will be used in a least-squares fitting procedure in order to derive the relative intensities of X-ray lines from experimental L X-ray spectra and to generate synthetic spectra to be used as references when experimental data are not available.

Experimental or synthetic reference spectra are required in order to derive the overlap correction factors and to express the net peak intensities in term of weight concentrations. For these purposes, reference compounds must be available. Synthetic lithium tetraphosphates (1), Ca-Al silicate glasses (7), pyrosilicates (26), or glassy garnets (5) bearing lanthanide elements can be used as reference materials for quantitative analysis by the use of the EPMA. Single oxide crystals are suitable materials to derive the data base allowing a complete description of X-ray spectra of the lanthanide elements. However, some crystals are difficult to prepare or are not stable and very often are available only in small quantities. Thus, when reference crystals are not available, reference spectra must be derived from experimental data derived from other materials.

This paper describes the lineshape of L X-ray spectra obtained by means of an automated EPMA equipped with WDS's. Particular attention is given to the X-ray emission spectra of the lanthanide elements. The effect of the natural width of X-ray lines on the resolution (peak width) of the observed X-ray peaks will be discussed, taking into account the intrinsic resolution of the spectrometer and the spectral distortions resulting from instrumental factors and from the existence of non-diagram lines. The characteristics of satellite lines accompanying the $L\beta_2$, $L\gamma_1$ and $L\gamma_2$ diagram lines will be given.

Response function of the wavelength dispersive spectrometer

Formalism

The observed photon energy distribution P(E) within an X-ray emission line may be expressed as :

$$P(E) = \int_{-\infty}^{+\infty} L(E')\, F(E - E')\, dE' = L(E) * F(E) \qquad [1]$$

where L(E) is the physical photon energy distribution and F(E) is the instrumental response function, E is the energy of the X-ray line and E' the variable energy.

The response function F(E) expresses the observed line shape of an incident monoenergetic photon assumed to have a natural width equal to zero or negligible with respect to the energy resolution of the spectrometer.

The natural width of an X-ray emission is generally well described according to a Lorentzian distribution :

$$L(E) = \frac{H}{1 + [(E-E_0)/\gamma]^2} \qquad [2]$$

where γ is the half width at half maximum (HWHM), H is the amplitude of the distribution centered at the energy, E_0.

Phillips and Marlow (17) studied K X-ray spectra in the 40-150 keV energy region using planar Ge and Ge(Li) detectors, and showed that for these detectors the response to monoenergetic incident radiation may be expressed according to :

$$F(E) = G(E) + S(E) + D(E) + B(E) \qquad [3]$$

where G(E) is the major Gaussian peak, S(E) represents the Compton scattering of photons and depends on the detector and the energy of the absorbed photons, B(E) is the continuum underlying the characteristic peaks and D(E) expresses the phenomena of incomplete charge collection occurring in the dead layer of the solid state detector. When a photon is partly absorbed in the inactive region of the detector, only part of the charge is collected. Pulses so generated have lower energies than the peak, leading to the development of a tail on the low energy side of the intense X-ray monoenergetic peak. Incomplete charge collection occurs mainly for low energy incident photons which are absorbed close to the detector window.

Within the 40-150 keV energy domain studied by Philips and Marlow (17), the natural width of K X-ray lines (50 - 100 eV) is comparable to the energy resolution of the Ge detector (400 - 500 eV). Thus, the main portion of the line shape is not a Gaussian but rather a Voigtian distribution. The observed peak shape, P (E), is the convolution product of F(E), the resolution function, with L(E), a Lorentzian distribution of unit area.

In order to determine the relative X-ray intensities of high energy K X-ray emission, Campbell et al. (3),(4) convoluted the response function with a Lorentzian of unit area.

Monoenergetic X-ray peaks measured with a Si(Li) detector are also well described by equation [3], as shown by Campbell et al. (4) who studied X-ray spectra in the range from 1 to 40 keV. Typically, the energy resolution of an EDS, within this energy domain is large compared to the few eV natural width of K X-ray peaks characteristic of low and medium Z elements and L X-rays of medium and high Z elements. Within the 1-40 keV energy region, the Lorentzian convolution can be omitted. The equations [1] and [3], describing the response function of the spectrometer, give an adequate representation of an X-ray peak observed by the use of a Si(Li) detector. In addition, Campbell et al. (3),(4) also showed that spectral distortion resulting from the Compton scattering is mainly restricted to X-ray photons of energy higher than $\simeq$ 20 keV. The tailing at energies from 1 to 15 keV may be attributed mainly to incomplete charge collection resulting from energy losses in the dead layer.

Empirical correction of the incomplete charge collection has been proposed for the case of EDS spectra induced by electron bombardment. However, in practice, the spectral distortion resulting from incomplete charge collection in EDS analysis with an EPMA is generally omitted and the line shape function is described by a single Gaussian distribution (9). In addition, the natural width of X-ray lines within the 1-20 keV energy domain is negligible with respect to the energy resolution of the Si(Li) detector (21) (22). Thus, the observed single Gaussian line shape is used in least-squares fitting techniques for EDS-EPMA data processing.

The situation is much more complex for the case of wavelength dispersive spectrometers (WDS) than that for EDS. Studying L X-ray spectra of the lanthanide elements by the use of WDS (LiF monochromator) Roeder (18) showed that a Gaussian distribution led to an approximate description of the peaks, except for tails that occur on each side of the peaks. Studying the fine structure accompanying the $L\beta_{2,15}$ and $L\gamma_1$ X-ray emission lines of the lanthanide elements (transitions originating from the incomplete 4 f shell), Salem and Scott (23) fitted their experimental data using the sum of two

Lorentzian shaped lines with two different widths. Similarly, the incompletely filled 3d shell of transition elements induces non-diagram lines associated with the $K\beta_{1,3}$ X-ray emission. Salem et al. (20) used a sum of Gaussian distributions as a fitting function to describe the observed photon energy distribution.

The observed shape of an X-ray line analyzed by means of WDS is controlled by the entrance slit of the spectrometer, the intrinsic properties of the monochromator and its geometrical arrangement within the spectrometer. Thus, there is no evidence that the line shape function (i.e., the net result of the spectrometer response function convoluted with the natural width of the line), satisfies a purely Gaussian or a purely Lorentzian distribution.

In practice, the line shape of an X-ray peak analyzed by means of WDS is between a Gaussian and a Lorentzian. Analyzing X-ray fluorescence peaks Huang and Lim (10) described the peak profile by the Voigt function, i.e., the convolution product of a Gaussian and a Lorentzian (equation [1]). In X-ray fluorescence analysis the peak position is usually given in terms of the angle of the diffracted X-ray beam, 2θ, with respect to the incident beam. The peak profile, $P(2\theta)$ may be thus expressed as follows :

$$P(2\theta) = H \int_{-\infty}^{+\infty} \left\{ \exp\left[-\ln 2 \left(\frac{2\theta'}{\Gamma_g} \right)^2 \right] . \frac{1}{1 + \left[\frac{(2\theta - 2\theta_0) - 2\theta'}{\Gamma_l} \right]^2} \right\} d(2\theta') \qquad [4]$$

where H and 2θ are the peak height and position of the analyzed radiation, Γ_g and Γ_l are the half widths at half maximum of the Gaussian and Lorentzian distributions, respectively. Although the resolution of the WDS is in most cases much better than that of an EDS, the Gaussian width, Γ_g (instrumental factor) is greater (or at least in the same order of magnitude) than the Lorentzian width, Γ_l (natural width). Thus, the profile of the peak is dominated by the Gaussian distribution, i.e., the instrumental response function. In order to study the natural width of L X-ray lines of the lanthanide elements, Salem and Lee (21) extended equation [4] above to equation [5] in order to account for the dependence of the entrance slit width, s, upon the peak shape. Keeping the notations used by Huang and Lim (10) in equation [4] the extended expression used by Salem and Lee (21) may be expressed by :

$$P(2\theta) = H \int_{-\infty}^{+\infty} \int_{2\theta - \frac{s}{2}}^{2\theta + \frac{s}{2}} \left\{ \exp\left[-\ln 2 \left(\frac{2\theta'}{\Gamma_g} \right)^2 \right] . \frac{1}{1 + \left[\frac{(2\theta - 2\theta_0) - 2\theta'}{\Gamma_l} \right]^2} \right\} d(2\theta)\, d(2\theta') \qquad [5]$$

Direct calculation of equations [4] and [5] is complicated and time consuming but will lead to an accurate fit of data. For practical use in quantitative processing of complex X-ray spectra by means of least-squares fitting techniques, Huang and Lim (10) suggested the replacement of the Voigt function with the following pseudo-Voigt function :

$$P(2\theta) = C_g\, G'(2\theta) + C_l\, L'(2\theta) \qquad [6]$$

where $0 \leq Cg \leq 1$ and $C_l = 1 - Cg$ are the contributions of the Gaussian $G'(2\theta)$ and Lorentzian $L'(2\theta)$ of same width, and centered at the position $(2\theta_0)$. Substituting the convolution product (equation [5] by the pseudo-Voigt function (equation [7]) greatly simplifies the fitting calculation (10).

Instrumentation and experimental procedure

The computer and microprocessor controlled CAMECA microprobe (Camebax Microbeam type) equipped with four WDS's and installed at the joint Bureau de Recherches Géologiques et Minières - Centre National de la Recherche Scientifique laboratory was used for this study. The WDS's are of the linear fully focusing type with a 40° take-off angle. The Rowland circle is 160 mm in diameter. The geometry of the linear focussing spectrometer

allows the take-off angle to be constant i.e. to be independent of the analyzed wavelength. Mechanical limitations allow the monochromator-detector assembly to vary continuously the sin θ values from 0.22400 to 0.82400, θ being the angle of the incident X-ray beam with respect to the surface of the monochromator. For the LiF (200) monochromator, (2d = 0.4026 nm), the analyzed wavelength domain varies from λ = 0.0902 nm to λ = 0.3318 nm. The monochromator is mounted to the spectrometer with a Johann mounting. According to this mounting, a flat crystal is bent to twice the focal circle radius so that the Bragg angle and focusing conditions are only approximately maintained. A deviation Δθ to the Bragg position, θ, increases the farther the incident X-ray beam is from the center of the monochromator. Thus, broadening and departure from symmetry of the peak shape will result from the monochromator mounting. The non-symmetry of peaks is easily observed for Bragg angles lower than 30°. The spectral characteristics of the analyzed X-ray lines will depend upon the area of the monochromator being illuminated by the incident X-ray beam. The active area of the crystal was reduced by covering the edge of the crystal with narrow bands of lead. The width (≈ 2 mm) of the lead strips was chosen in order to obtain a compromise between the gain in energy resolution and the loss in detection efficiency. In addition, reducing the active area of the crystal results in a less pronounced peak distortion.

In order to derive a mathematical description of the peak shape, monochromatic L X-ray emissions for lanthanide elements and for Au, W and Pt were analyzed by means of the LiF monochromator were digitally recorded. An interval corresponding to a variation of ± 0.001 of the sin θ value around the peak maximum was analyzed by moving the monochromator step by step. Each step was equal to an increase of Δ sin θ = $2\ 10^{-5}$ so that each analyzed wavelength domain contained one thousand channels. For each channel, the counting time was 0.5 sec. The primary beam energy was 25 keV with a 30 nA beam current was used. Data acquisition was carried out using integral mode of the pulse height analyzer.

For some data, the Cameca MS 46 instrument installed at the Laboratoire de Petrologie Mineralogique in the University Pierre and Marie Curie in Paris was used. The spectrometers are of the linear fully focusing type with a take-off angle of 18°. The quartz $(10\bar{1}1)$ monochromator (2d = 0.6686 nm) is set according to the Johansson mounting so that the Bragg angle is satisfied for any incident X-ray beam at the surface of the monochromator. The resolution is improved by a factor of ≈ 2 compared to the resolution obtained with the same spectrometer with a LiF monochromator with Johann mounting.

The EPMA equipped with the quartz monochromator (Johansson mounting) was only used for qualitative purposes in order to validate the existence of multiple lines that were not sufficiently resolved by the use of the first type of spectrometer and to assign peak asymmetry either to instrumental factors or to the presence of non-diagram lines respectively.

Only spectra obtained with the LiF monochromator were digitally recorded and processed by a least-squares fitting technique using a pure Gaussian, a pure Lorentzian or a linear combination of both distributions.

In order to account for a possible deviation from symmetry of the peaks, Huang and Lim (10) varied the half-width, W, of the Gaussian and Lorentzian distributions in the pseudo-Voigt fitting function so that :

$$W = W_r \text{ if } 2\theta > 2\theta_0 \text{ and,}$$
$$W = W_e \text{ if } 2\theta < 2\theta_0 \qquad [7]$$

where, $2\theta_0$ is the monochromator position associated with the peak maximum.

This approach is based on a single analytical description of the peak and the spectral distortion is different from the approach used in EDS data processing based on the Hypermet function (equation [3]) in which the line shape of the X-ray emission and the spectral distortion are described by means of separate analytical expressions.

We adopted an approach similar to that used in the Hypermet function (equation [3]) and described the WDS peak shape according to a linear expression of the following form :

$$P(\lambda) = k\, P_1(\lambda) + (1 - k)\, P_2(\lambda) + G(SP, \lambda) \qquad [8]$$

with

$$P_1(\lambda) = H \exp\left[-\ln 2 \left(\frac{\lambda-\lambda_0}{\Gamma(\lambda_0)}\right)^2\right], \qquad [9]$$

$$P_2(\lambda) = \frac{H}{1 + [(\lambda-\lambda_0)/\Gamma(\lambda_0)]^2}\ . \qquad [10]$$

where $P_1(\lambda)$ and $P_2(\lambda)$ are a Gaussian and a Lorentzian distribution, respectively centered at wavelength λ_0, with the same amplitude H, and half width $\Gamma(\lambda_0)$ and in relative proportion k and (1-k), respectively ; G (SP) is a function to be determined in order to account for spectral distortions.

The adjustment of fit of the experimental spectra to the model function (sum of a base line and Gaussian/Lorentzian lines) has been done with an automated fitting program, minimizing the residual distance normalized to the number of data point (Standard Deviation, equation [11]).

$$SD = \left[\Sigma \frac{[P'(\lambda_i) - P(\lambda_i)]^2}{n} \right]^{1/2} \qquad [11]$$

where n is the number of considered data points, $P'(\lambda_i)$ is the number of count at λ_i and $P(\lambda_i)$ is the value of the model function at that point. Due to the non-linearity of the model function (Gaussian or Lorentzian) towards the adaptable parameters (amplitude, half-width at half-maximum, position) the automatic fitting procedure requires an iterative computation, starting on an estimated solution. This has been done using a modified iterative non-linear least square fitting process. Each adaptable parameter can be fixed, released or coupled to others to ensure a proper modeling of the spectrum taking into account its known properties (known position, known ratios between two intensities, known distance between two peaks etc...). The program we developed, written in C programming language, is running on PC compatible equipment and can deal with a maximum of 4096 points at a time, it includes both interactive graphic interface and automatic fitting procedure. It is already used for fitting a wide range of spectroscopic data (16).

Materials studied

In order to provide an analytical description of L X-ray spectra of the lanthanide elements, the materials used in this study are Ln_2O_3 single crystals. These crystals were prepared at the Ecole Nationale Superieure de Chimie de Paris (ENSCP) using the Verneuil crystal growth method (14). Starting from oxide powders the following crystals were prepared by a reducing flame :

Hexagonal crystals : La_2O_3, Pr_2O_3, Nd_2O_3.
Monoclinic crystals : Sm_2O_3, Eu_2O_3, Gd_2O_3
Cubic crystals : Dy_2O_3, Ho_2O_3, Er_2O_3, Yb_2O_3

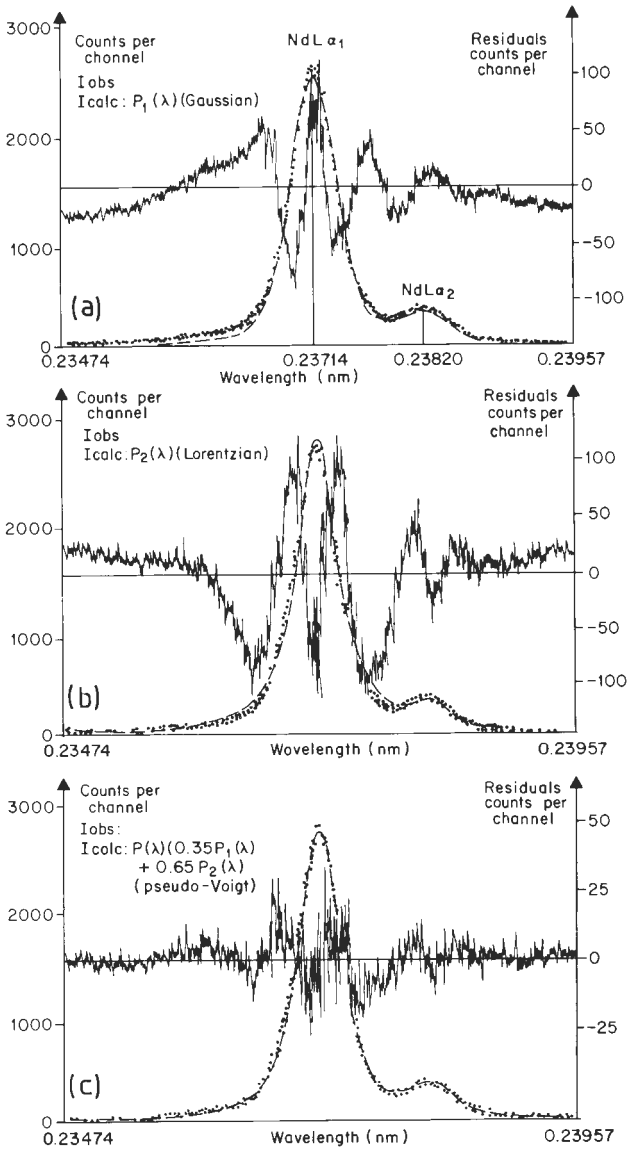

Figure 1. Results of fits to the Nd $L\alpha_1$, α_2 peaks and residuals using (a) a pure Gaussian [$P_1(\lambda)$], (b) a pure Lorentzian [$P_2(\lambda)$], and (c) a linear combination of both [$P(\lambda) = 0.35\ P_1(\lambda) + 0.65\ P_2(\lambda)$] as successive fitting function.

Owing to their high sensitivity to air and humidity, raw crystals and polished sections of La_2O_3, Pr_2O_3, Nd_2O_3, Sm_2O_3 and Eu_2O_3 were kept in a vacuum sealed desiccator. Chips of a few millimeters square in size were prepared as polished specimens for EPMA analysis. The materials were embedded in an araldite epoxy and kept in a vacuum during polymerization of the resin. The specimens were first ground by means of SiC abrasives decreasing from 12 to 5 microns in size and then polished on an aluminum plate using diamond abrasives (3 microns and one micron) dispersed in oil. The surfaces were polished again on a polishing cloth using 0.5 micron diamond.

Hexagonal and monoclinic crystals have a layered structure and are easily cleaved under mechanical strength. For hexagonal crystals, the direction of the growth-axis depends upon the rate of growth but is generally close to that of the c-axis. Thus, the cleavage plane is (001). For crystals having a monoclinic structure, cleavage always occurs along (201). It is difficult to mechanically polish sheet-layered specimens along the cleavage plane since peeling or smearing effects often take place leading to damaged surfaces. The specimens were first polished along the cleavage plane according to the procedure described above. The specimens were then cut perpendicular to the polished surface, i.e., parallel to the c-axis, rotated by an angle of 90°, embedded in resin and polished to obtain a surface orientated perpendicular to the cleavage plane.

In addition, the pure elements Au, W and Pt were analyzed in order to investigate X-ray emissions of short wavelength which are detectable with a LiF monochromator.

The line shape description of Lα peaks analyzed by means of the LiF monochromator :

In order to determine the analytical expression describing the Lα X-ray peaks observed using the LiF monochromator, experimental data were processed using equation [8] as the fitting function. The term, G(SP, λ), in equation [8] was first omitted in the fitting procedure. The value of coefficient k, was varied from k = 0 (pure Lorentzian) to k = 1 (pure Gaussian). The continuous emission underlying each monoenergetic peak was assumed to be linear as a function of wavelength. The peak height, the HWHM and the maximum position of the Gaussian and Lorentzian distributions were used as variables in the fitting procedure. Results are illustrated in Fig.1 for the case of the Nd $L\alpha_1$, $L\alpha_2$ X-ray peaks (0.2371 nm and 0.2381 nm respectively) occurring for a medium position of the monochromator within its total range.

As shown in Fig.1, neither a pure Gaussian distribution ($P_1(\lambda)$, k = 1) nor a pure Lorentzian distribution ($P_2(\lambda)$, k = 0) led to an accurate description of the analyzed X-ray peak. The calculated HWHM values and peak positions were consistent whether a pure Gaussian or a pure Lorentzian was used as a fitting function. However, a pure Gaussian distribution led to a calculated peak height slightly lower than the measured intensity while the opposite was encountered when a pure Lorentzian distribution was used. In addition, discrepancies between experimental and theoretical distributions became apparent at both tails of the peak.

Although there is no physical basis to support the assumption that the peak shape results from a linear combination of a Gaussian and a Lorentzian distribution, the Nd $L\alpha_1$ peak is correctly described (see Fig.1) by the polynomial expression (equation [8]) in which the k parameter was set to k = 0.35. This resulted in the smallest SD value for the fitting procedure. However, the k value leading to the best fit was found to vary as a function of the analyzed wavelength. The optimum k value decreases exponentially from k = 0.6 at short wavelengths ($\lambda \approx 0.12$ nm) down to k = 0.35 at medium wavelengths ($\lambda \approx 0.22$ nm) and tends to be constant at $k \approx 0.30$ for greater wavelengths.

Varying the value of k does not change substantially the calculated HWHM values. For example, the HWHM for Au Lα (0.1276 nm) is only decreased by less than 1 % when the value of k is increased from k = 0.35 to k = 0.50, the latter leading to the best fit.

As shown in Fig. 2, the calculated HWHM values (k = 0.35) of the $L\alpha_1$ peaks linearly varied with wavelength for wavelengths greater than ≃ 0.17 nm. For the LiF monochromator used and a value of k = 0.35, the variation of $\Gamma(\lambda)$ as a function of wavelength satisfied the following linear relation :

$$\Gamma(\lambda) = (-0.89\ \lambda + 0.47)10^{-3} (\lambda > 0.17 \text{ nm}) \quad [12]$$

For wavelengths less than ≃ 0.17 nm, and using the pseudo-Voigt function (equation [8] with k = 0.35 and G (SP, λ′) = 0) the

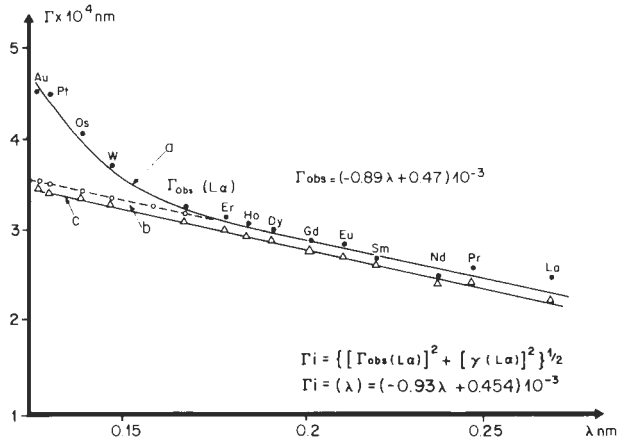

Figure 2. Variation of the HWHM of $L\alpha_1$ peaks (LiF monochromator) as a function of wavelengths.
a) Calculated half-widths using the pseudo-Voigt function $P(\lambda) = 0.35\ P_1(\lambda) + 0.65\ P_2(\lambda)$ as the fitting function (equations [9] and [10]).
b) Peaks half-widths corrected for the spectral distortion resulting from instrumental factors (equations [13] and [14]).
c) Calculated instrumental resolution function Γi, of the spectrometer derived from the calculated Lα peak half-widths and the natural half-width of the analyzed emission according to equation [20].

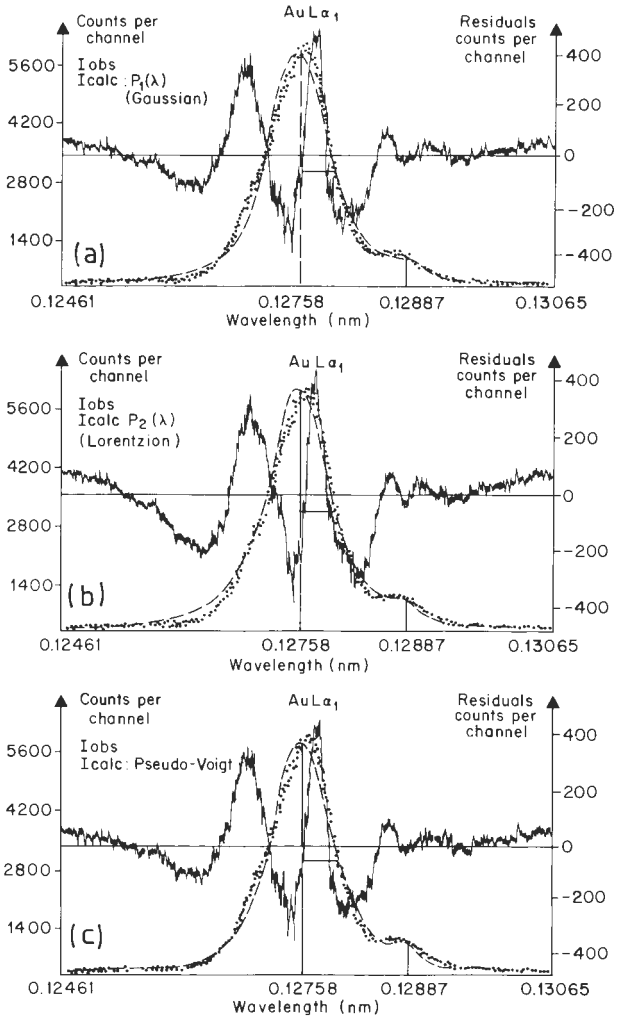

Figure 3. Results of fits to the Au $L\alpha_1$, α_2 peaks and residuals according to the same procedure as in Fig. 1.

calculated Γ(λ) values decreased approximately exponentially in the wavelength range of 0.11 nm to 0.17 nm.

For all analyzed Lα peaks, modifying the k value i.e. the relative proportion of Gaussian and Lorentzian distributions contained in the pseudo-Voigt fitting function, leads to a more or less acceptable description of the peak tails on both sides of the peaks. This in turn led to a poor value of the SD value of the fit. In addition, for Lα peaks with wavelength less than ≃ 0.17 nm (exponential decay of the Γ(λ) curve in Fig.2), the calculated peak position did not correspond to the observed maximum position. This deviation occurred for all values of k used in the fitting function. Such an effect is illustrated in Fig. 3 for the case of the Au $L\alpha_1$ peak. Since both the Gaussian and Lorentzian contributions are symmetrical functions with the maximum centered on the same channel, the deviation between the observed and calculated maximum positions indicates an asymmetrical line shape. As previously mentioned an asymmetrical shape is expected for peaks occurring at low Bragg angles.

For wavelengths less than ≃ 0.17 nm, the departure from linear dependence shown on the Γ(λ) vs λ curve in Fig.2 was associated with spectral distortion resulting from instrumental factors. This conclusion was supported by comparison of spectra recorded using the LiF (Johann mounting) and the quartz (Johansson mounting) monochromators. The HWHM

of peaks observed with the quartz crystal was found to be improved by a factor ≃ 2 with respect to the resolution of the LiF monochromator. When using the quartz monochromator the spectra were only recorded in analog mode and it was not possible to analytically describe the peak shape. However, the Lα peaks occurring at wavelengths less than ≃ 0.17 nm remained apparently symmetrical compared to the Lα peaks obtained by means of the LiF monochromator.

For wavelengths less than ≃ 0.17 nm, the best fit of the Lα peaks (LiF monochromator) was obtained by increasing the fraction, k, of Gaussian distribution contained in the linear pseudo-Voigt fitting function given by equation [8]. Thus, we assumed that the instrumental factors modifying the peak shape can be empirically described by a Gaussian distribution.

A Gaussian distribution $G(SP, \lambda'_0)$ was consequently added to the pseudo-Voigt fitting function, in which the k value was set to k = 0.35 for all wavelengths analyzed with the LiF monochromator.

The complete fitting function describing the peak shape was thus :

$$P(\lambda) = 0.35\ P_1(\lambda) + 0.65\ P_2(\lambda) + G(SP, \lambda') \quad [13]$$

where $P_1(\lambda)$ and $P_2(\lambda)$ represent a Gaussian and a Lorentzian distribution respectively with the same amplitude and width (equations [9] and [10]) and $G(SP,\lambda')$ being expressed by :

$$G(SP, \lambda) = H(SP, \lambda') \exp\left[-\ln 2 \left(\frac{\lambda-\lambda'}{\Gamma(SP)}\right)^2\right] \quad [14]$$

where $H(SP, \lambda')$ is the amplitude of the Gaussian centered at wavelength λ', with a HWHM value $\Gamma(SP,\lambda')$, and λ the wavelength of the analyzed monochromatic X-ray emission (7).

The digitally recorded Lα peaks occurring at wavelengths lower than 0.17 nm were processed by using equations [13] and [14] as a complete fitting function which contains six variables, i.e., the peak height, the peak position and the HWHM describing the X-ray peak (pseudo-Voigt function), the amplitude $H(SP,\lambda')$, the HWHM, $\Gamma(SP,\lambda')$ and the maximum position, λ', of the Gaussian (equation [14]) describing the spectral distortion of the peaks.

Results in Fig.4 illustrate the observed Au $L\alpha_1$ peak shape as the sum of two distributions associated with the pseudo-Voigt function (instrumental line profile) and the Gaussian function (spectral distortion resulting from the monochromator mounting) which are included in the fitting function given by equations [13] and [14].

For wavelengths greater than ≃ 0.17 nm the amplitude of the Gaussian $G(SP,\lambda')$ becomes negligible with respect to the amplitude of the characteristic X-ray line. For Lα peaks with wavelengths less than 0.17 nm, the maximum position, the amplitude and the HWHM $\Gamma(SP)$, of the Gaussian, $G(SP, \lambda')$ may be expressed as a function of the parameters of the major characteristic peak according to the following relations :

$$\lambda' - \lambda = -0.87\ 10^{-3} \exp[-3.4\ \lambda] \quad [15]$$

$$\frac{H(SP, \lambda')}{H(P, \lambda)} = 2930 \exp[-3.6\ \lambda] \quad [16]$$

$$\Gamma(SP, \lambda') = 8.6\ 10^{-3} \exp[-24\ \lambda'] \quad [17]$$

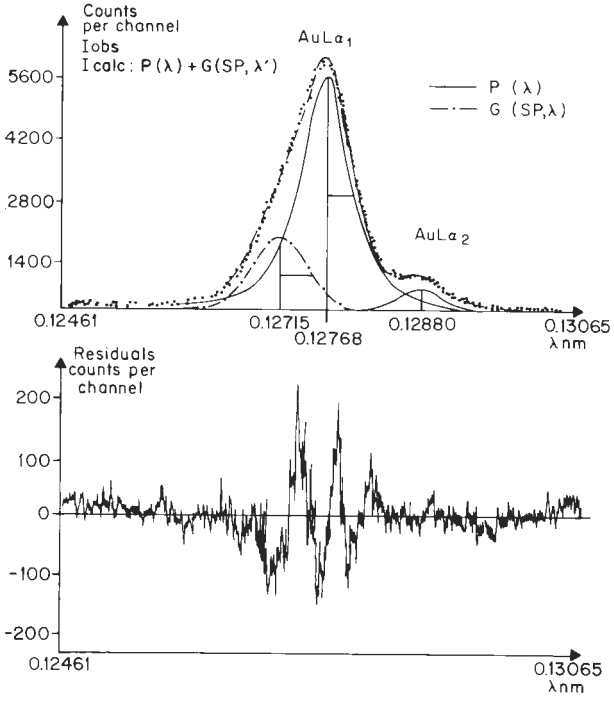

Figure 4. Results of fit to the Au $L\alpha_1$, α_2 peaks (upper trace) and residuals (lower trace) using the pseudo-Voigt function and a Gaussian offset as fitting function (see equation [13] and [14]).

The instrumental resolution function of the LiF monochromator

The observed shape of L α_1 peaks resulting from the use of the LiF monochromator is correctly described by a pseudo-Voigt function, i.e., a linear combination of a Gaussian distribution and a Lorentzian distribution, both distributions being centered on the same wavelength and having the same width. This theoretical description of WDS X-ray peaks analyzed by means of the EPMA is consistent with the description of XRF peaks as reported by Huang and Lim (10). In the present study, fractions of 0.35 Gaussian and 0.65 Lorentzian were found to match the observed peaks. Monoenergetic peaks occurring at wavelengths less than ≃ 0.17 nm exhibited an asymmetrical shape with a shoulder occurring on the short wavelength side of the peak. This spectral distortion resulting from instrumental factors was described by a Gaussian offset.

The effect of the instrumental factor upon the peak shape being corrected, a linear variation of the HWHM of the peak vs the wavelength was observed, consistent with the results reported by Roeder (18).

The calculated Γ value is an effective HWHM value resulting from effect of the intrinsic instrumental resolution Γ_i, and the natural half width γ, of the analyzed X-ray emission.

The two parameters, Γ_i and γ, are only treated individually by the use of the convolution product expressed by equation [1] where the instrumental response function vs energy F(E), contains the intrinsic resolution Γ_i, and the physical X-ray photon distribution, L(E), is expressed in terms of the natural half width γ. Thus, the rigorous approach consisting in the convolution product assuming that the instrumental response function F(E) is known would lead to an expression of the observed peak profile P(E) containing both Γ_i and γ factors as variables.

Similarly, the simplified model based on the use of a pseudo-Voigt function should be expressed in terms of both Γ_i and γ values rather than in terms of the effective resolution factor Γ. Thus, the complete fitting function in equation [13] should be written as :

$$P(\lambda) = P(\Gamma_i, \gamma, \lambda) \qquad [18]$$

When a Gaussian is convoluted with another Gaussian the resulting HWHM can be obtained by quadratic additions of the HWHM values of each distribution. We numerically verified that the HWHM, Γ, obtained by convoluting a Gaussian $G(\Gamma_G)$ with a Lorentzian distribution of unit area $L(\Gamma_L)$ is close in a first approximation to the quadrature addition of the HWHM values Γ_g and Γ_L, respectively, so that :

$$\Gamma(G * L) \simeq [(\Gamma_g)^2 + (\Gamma_L)^2]^{1/2} \qquad [19]$$

For example, the natural width of the Nd Lα, emission is 3.93 eV equivalent to 0.178 10^{-3} nm ($\Delta E = (hc/\lambda^2)\,\Delta\lambda$) which corresponds to 36 % of the calculated width Γ_g of the peak (10.9 eV or 0.494 10^{-3} nm) which was assumed to have a pure Gaussian distribution. The curve resulting from the convolution product of the Gaussian with a Lorentzian distribution of unit area and HWHM, Γ_L, equal to the natural width of the Nd Lα_1 emission was characterized by a HWHM, Γ (G * L) equal to 11.9 eV or 0.542 10^{-3} nm. The HWHM calculated by quadrature addition of the Γ_g and Γ_L values according to equation [19] leads to a HWHM value of 11.6 eV or 0.524 10^{-3} nm, which differs only by 3 % from the measured HWHM value, Γ(G * L).

Any X-ray emission peak, being corrected for instrumental spectral distortion can be described by a pseudo-Voigt function with an effective HWHM expressed as :

$$\Gamma_{jk} = [(\Gamma_i)^2 + (\gamma_{jk})^2]^{1/2} \qquad [20]$$

where

. Γ_{jk} is the observed half-width of the peak resulting from the radiative transition between the j and k levels, respectively;
. Γ_i is the HWHM value resulting from the instrumental resolution of the spectrometer;
. γ_{jk} is the natural half width of the jk X-ray emission line.

The instrumental resolution $\Gamma_i(\lambda)$ is derived from equation [20] using the linear variation vs wavelength of the calculated Γ (Lα) width of the Lα peaks of pure elements and lanthanide oxide crystals (equation [12]) and the corresponding natural half-width γ (Lα) according to Salem and Lee (21),(22).

As shown in Fig. 2, a linear variation for Γ_i vs wavelength was observed according to:

$$\Gamma_i(\lambda) = (-0.93\,\lambda + 0.466)\ 10^{-3}\ \text{nm} \qquad [21]$$

Application to L X-ray spectra of the lanthanide elements

Results

$L\alpha_1$ and $L\alpha_2$ X-ray peaks of some of the lanthanide elements were processed using the pseudo-Voigt function as a fitting function. The calculated data showed a linear correlation for HWHM vs wavelength of the peaks. Simultaneously the peak heights of the $L\alpha_1$ and $L\alpha_2$ peaks exhibited a linear variation as a function of wavelength.

The $L\beta_1$, $L\beta_2$, $L\beta_3$, $L\beta_4$, $L\beta_6$, $L\gamma_1$, $L\gamma_2$, $L\gamma_3$ and Ll emission peaks were processed keeping the peak position, peak width and peak height as variables in the fitting procedure. The variation in observed HWHM vs wavelength of the peaks exhibited an array as shown in Fig 5. We examined the effect of spectral distortions and natural width of emission lines upon the calculated HWHM values for the different $L\beta$, $L\gamma$ and Ll emission lines.

<u>$L\beta$ lines and satellites</u> : When the atomic number of the lanthanide elements is increased, the $L\beta_4$ emission peak moves from the short wavelength side of the $L\beta_1$ peak towards the long wavelength side of the $L\beta_1$ peaks as illustrated in Fig 6. Owing to the energy resolution of the spectrometer the $L\beta_4$ and $L\beta_1$ peaks cannot be distinguished for the cases of Nd and Sm. For the case of Gd, the $L\beta_4$ peak appears as a shoulder of the $L\beta_1$ peak and both peaks are seen individually when the atomic number of the element is increased. The calculated effective widths for the $L\beta_1$ and $L\beta_4$ emission peaks were found to vary linearly as a function of the wavelength. As shown in Fig.5, the HWHM values of the $L\beta_1$ peaks satisfy the same linear variation vs wavelength as that observed for the case of the $L\alpha_1$, peaks. This similarity in the relationships of the $L\beta_1$, $L\alpha_1$ and $L\alpha_2$ peak widths vs the wavelength is consistent with the similarity in the natural widths of these X-ray emissions as illustrated in Fig.7. The widths of the $L\beta_4$ peaks were found to be slightly higher than these of the $L\alpha_1$ peaks of equivalent wavelength. This observation is consistent with the difference in natural widths of the X-ray emissions. For overlap corrected $L\beta_4$ and $L\beta_1$ peaks, the intensity dependence vs the wavelength was linear for both $L\beta_1$ and $L\beta_4$ X-ray emission peak as shown in Fig.8.

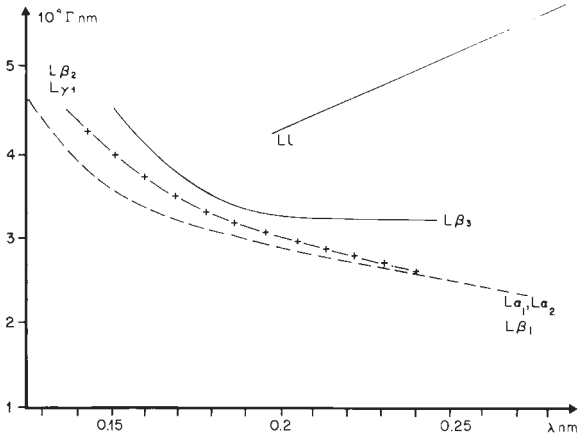

Figure 5. Observed HWHM of peaks for some of the L emission lines of the lanthanide elements (data not corrected for spectral distortions).

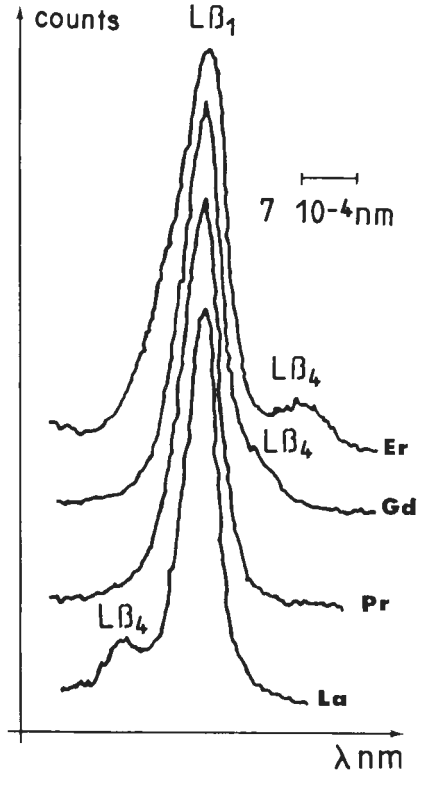

Figure 6. Relative position of the $L\beta_4$ emission peak with respect to the $L\beta_1$ emission peak of some lanthanide elements.

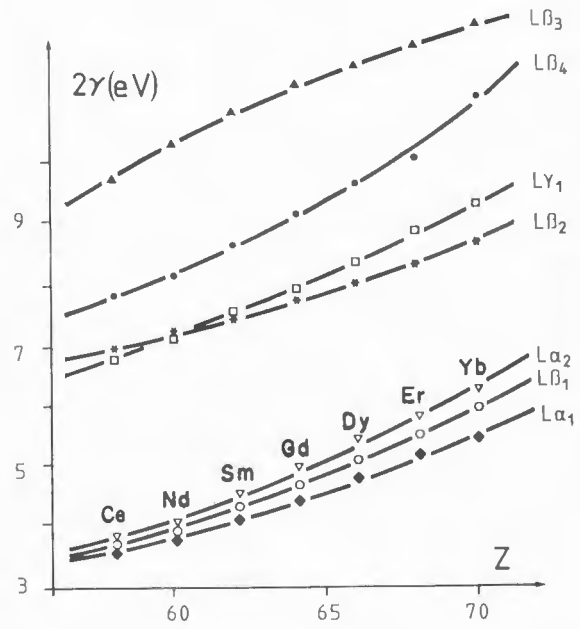

Figure 7. Natural width 2γ, in eV, of some L X-ray emission lines of the lanthanide elements according to Salem and Lee (21).

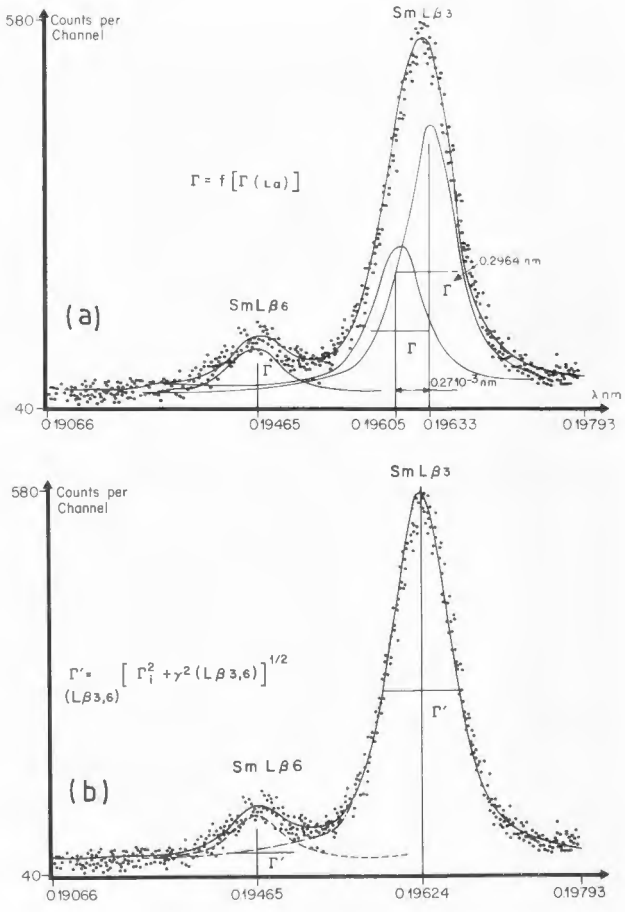

Figure 9. Results of fits to the SmLβ_3 peak analyzed by means of the LiF monochromator.
a) Least-squares fitting procedure using the Lβ_3 peak half-width Γ_1, derived from the $\Gamma(L\alpha) = f(\lambda)$ curve (see Fig. 2 and equation [12]).
b) Least-squares fitting procedure using the Lβ_3 peak half width Γ_2, derived from equation [20] taking into account both the instrumental resolution Γ_i (equation [21]) and the natural width $\gamma(L\beta_3)$ (Fig. 7).

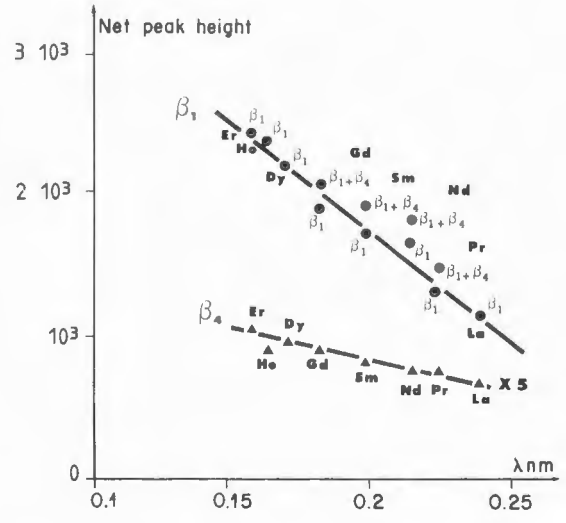

Figure 8. Linear variation of the Lβ_1 and Lβ_4 peak heights of the lanthanide elements as a function of wavelength.

A similar relationship than that observed between the Lβ_1 and Lβ_4 peaks is encountered for the case of the Lβ_3 and Lβ_6 X-ray emission peaks. For light lanthanide elements the Lβ_6 peak occurs at a shorter wavelength than that of the Lβ_3 peak. When the atomic number of the analyzed element is increased the Lβ_6 -Lβ_3 distance decreases and becomes equal to zero for the case of Dy (Z = 66) then the wavelength difference becomes positive, i.e., the Lβ_6 peak occurs at greater wavelength than that of the Lβ_3 peak.

Only $L\beta_3$ - $L\beta_6$ emission peaks for elements with atomic number $57 \leq Z \leq 64$ were processed by means of the least-squares fitting technique. For elements with an atomic number greater than Z = 65 the solution to peak overlap correction was made difficult by the severe instrumental spectral distortions affecting both peaks. Peak width and peak intensity of the heavy lanthanide elements were extrapolated from calculated data for $Z \leq 64$ (Gd). Therefore, extrapolated data were used to generate synthetic spectra which were found to correctly describe the experimental spectra, justifying in turn the extrapolation approach.

For the $L\beta_6$ emission peaks, the calculated HWHM values (corrected for spectral distortion) were found to vary linearly as a function of wavelength. Taking into account the large difference in statistical fluctuations in $L\alpha_1$ and $L\beta_6$ peak intensities, the calculated widths of the $L\beta_6$ peaks were found equivalent, to a first approximation to those of the $L\alpha_1$ peaks of equivalent wavelength.

As shown in Fig.5 the relationship between wavelength and observed HWHM for $L\beta_3$ peaks strongly differs from that of the $L\alpha_1$ peak. The $L\beta_3$ -$L\beta_6$ peak overlap is not sufficient to explain the greater peak widths for $L\beta_3$ peaks with respect to $L\alpha_1$ peaks.

It was thus tempting to identify the $L\beta_3$ peak broadening as the result of two unresolved lines as shown in Fig.9a. For these calculations the HWHM of the two components were set at the values, $\Gamma_1 = f(\Gamma(L\alpha))$, derived from equation [12]. Such deconvolution of the $L\beta_3$ peak led to the detection of spurious peaks since the $L\beta_3$ is a single line as shown in Fig 9b. For the case of data in Fig. 9b the HWM values, $\Gamma_2(L\beta_3)$, were calculated according to equation [20] including the instrumental resolution of the spectrometer, $\Gamma_i(\lambda)$, (equation [21]) and the natural half-width values, $2\gamma(L\beta_3)$, published by Salem and Lee (21),(22). The natural widths of the $L\beta_3$ peaks are approximately twice those of the $L\alpha_1$ peaks for the lanthanide elements as shown in Fig 7. These differences are responsible for the observed variations of the peak width as a function of the $L\beta_3$ analyzed wavelength. Comparisons of observed (least-squares fitting procedure) and calculated HWHM are shown in Table 1. The values, Γ_1, are derived from the calibration curve drawn for $L\alpha$ emission lines. The calculated, Γ_2 values accounting for the natural peak widths are in a good agreement with the measured HWHM of the peaks. Consistent with the results reported for the $L\alpha_1$, $L\alpha_2$, $L\beta_1$ and $L\beta_4$ emission peaks, the intensities of the $L\beta_3$ and $L\beta_6$ peaks also varied linearly with wavelength.

The $L\beta_2$ emission peaks for La, Pr, and Nd were correctly described by means of the fitting function (equation [13]) leading to a calculated width consistent with those of $L\alpha$ peaks of equivalent wavelength. However at greater atomic numbers, (e.g. 64 (Gd)), the $L\beta_2$ peak broadened and a shoulder becomes visible on the long wavelength side of the peak as shown in Fig.10.

Table 1. Observed and calculated HWHM values (nm) for the $L\beta_3$ emission peak of some lanthanide elements.

	La	Ce	Pr	Nd	Sm	Eu	Gd	Dy	Ho
$\lambda(L\beta_3)$	0.2411	0.2311	0.2218	0.2127	0.1963	0.1887	0.1815	0.1683	0.1621
$\Gamma_1 = f(\Gamma(L\alpha))$ equation [12]	0.255 10^{-3}	0.265 10^{-3}	0.273 10^{-3}	0.280 10^{-3}	0.295 10^{-3}	0.302 10^{-3}	0.308 10^{-3}	0.320 10^{-3}	0.326 10^{-3}
$\Gamma_2 = \sqrt{\Gamma_i^2 + \gamma^2}$	0.326 10^{-3}	0.326 10^{-3}	0.327 10^{-3}	0.330 10^{-3}	0.336 10^{-3}	0.340 10^{-3}	0.346 10^{-3}	0.367 10^{-3}	0.373 10^{-3}
Γ^*_{obs}	0.330 10^{-3}	not measured	0.320 10^{-3}	0.328 10^{-3}	0.334 10^{-3}	0.338 10^{-3}	0.366 10^{-3}	0.372 10^{-3}	0.40 10^{-3}

* (including spectral distortion resulting from the monochromator mounting).

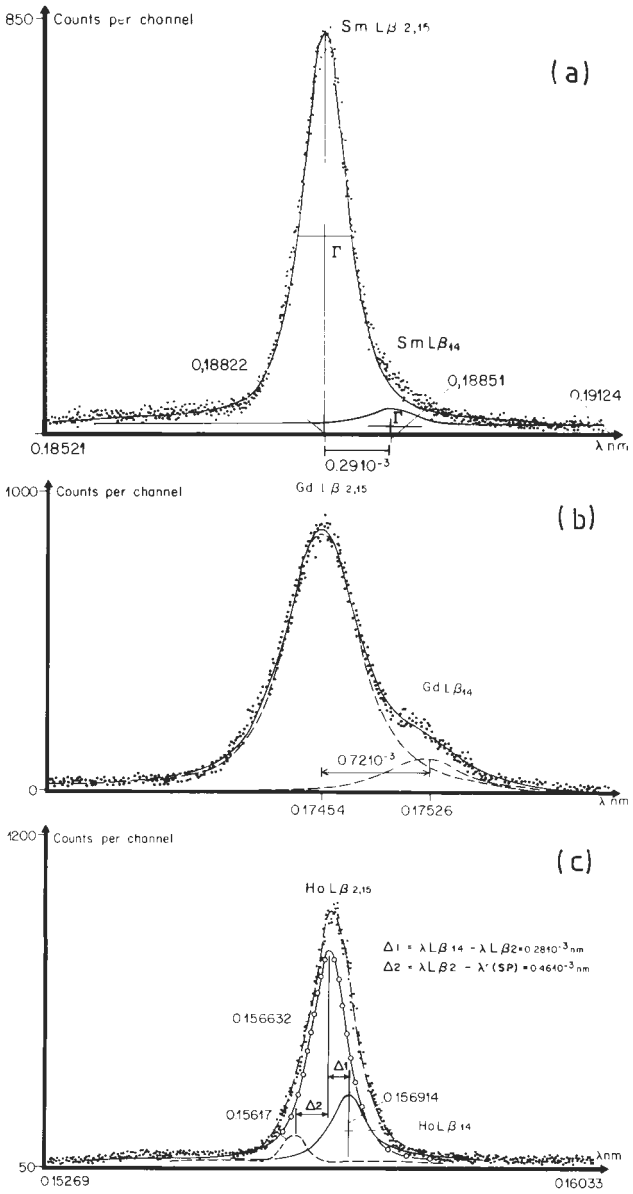

Figure 10. $L\beta_2,\beta_{15}$ doublet emission peak profiles indicating the existence of a non-diagram line, $L\beta_{14}$, on the long wavelength side of the $L\beta_2$ diagram line : (a) Sm $L\beta_2$, (b) Gd $L\beta_2$, (c) Ho $L\beta_2$.

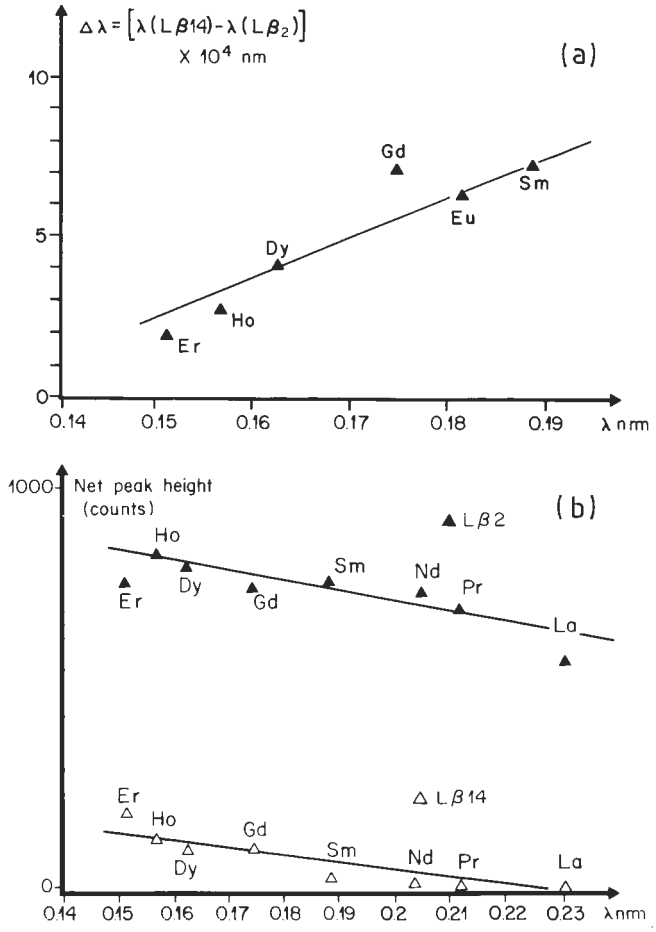

Figure 11. (a) wavelength distance separation $L\beta_{14}$ - $L\beta_2$ variation and (b) intensity variation of the $L\beta_2$ and $L\beta_{14}$ peaks, as a functions of wavelength.

For the analyzed $L\beta_2$ peaks for Sm, Eu, Gd, Dy, Ho and Er, the deconvolution procedure showed the existence of a second peak, labelled $L\beta_{14}$. The $L\beta_{14}$ peak occurs on the long wavelength side of the major $L\beta_2$ peak. For the calculations, the HWHM of both peaks were set at the same value. As shown in Fig. 10 the Ho $L\beta_2$ shape was corrected for the spectral distortion but such correction was neglected for the case of the second peak β_{14}, of low intensity. A similar deconvolution procedure was applied to all analyzed $L\beta_2$ peaks. However, based on these simplifications the calculated separation distance between the $L\beta_2$ and $L\beta_{14}$ peaks decreased linearly as a function of wavelength as shown in Fig. 11a. The width of the Gd $L\beta_{14}$ was found to be greater than that of the $L\beta_{14}$ of the other elements. As shown in Fig. 11b height the amplitude of the $L\beta_2$ and $L\beta_{14}$ peaks increased linearly with wavelength.

The $L\beta_2$ emission results from the L_{III} N_{IV} transition and its energy is very close to that of the $L\beta_{15}$ emission which results from the L_{III} N_V transition. Only a few data are available in the literature about the $L\beta_{15}$ wavelength of the elements. However, the characteristic wavelength associated with the $L\beta_{15}$ emission line can easily be calculated.

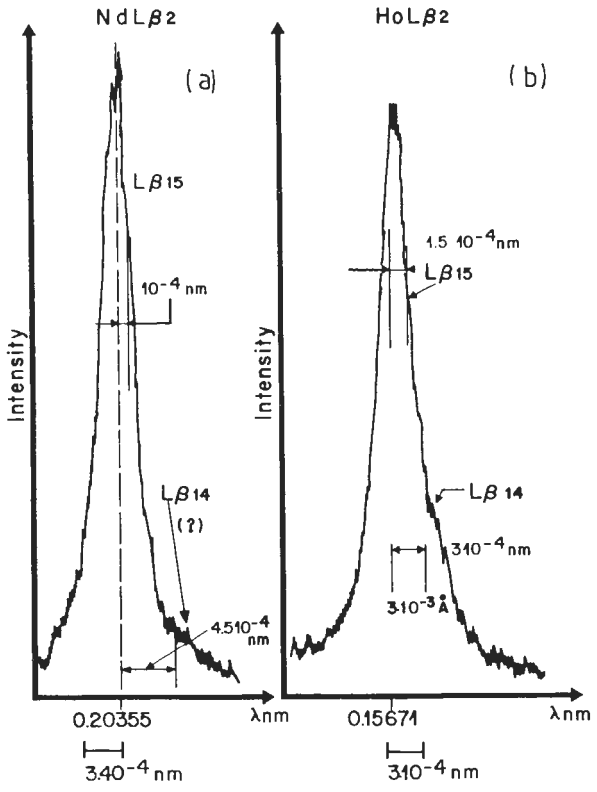

Figure 12. $L\beta_{2,15}$ diagram lines and $L\beta_{14}$ non-diagram-line analyzed by means of the quartz monochromator (Johansson mounting) for the case of (a) Nd, and (b) Ho.

Both the $L\gamma_1$ and $L\beta_{15}$ emissions result from transitions originating from the N_{IV} level so that the $E(L\gamma_1) - E(L\beta_{15})$ energy difference is equal to the difference between the final levels involved in the radiative transitions so that :

$$E(L\gamma_1) - E(L\beta_{15}) = E(L_{II}) - E(L_{III}) \quad [22]$$

The energy difference $E(L_{II}) - E(L_{III})$ also equals the energy difference between the $K\alpha_2$ and $K\alpha_1$ monoenergetic radiations which correspond to the same final levels and originate from the L_{II} and L_{III} levels, respectively.

Thus, the energy of the $L\beta_{15}$ emission line can be derived from the tabulated $L\gamma_1$, $K\alpha_1$, and $K\alpha_2$ data according to:

$$E(L\gamma_1) - E(L\beta_{15}) = E(K\alpha_1) - E(K\alpha_2) \quad [23]$$

Using published data for the above photon energies (6) the wavelength distances between the $L\beta_2$ and $L\beta_{15}$ emission lines were calculated for the case of the lanthanide elements. These calculations showed that the wavelength separation, $L\beta_2 - L\beta_{15}$, increased from $\simeq$ 0.00010 nm to $\simeq$ 0.00025 nm. These values are lower than the instrumental resolution of the spectrometer equipped with the LiF monochromator. Thus, the $L\beta_2$, $L\beta_{15}$ doublet, associated with the major peak in (Fig.10) is not resolved and the observed feature on the long wavelength side of the unresolved $L\beta_{2,15}$ peak corresponds to a non-diagram line. This satellite peak was labelled as $L\beta_{14}$, consistent with the notations used by Sakellaridis (19) (see chapter Discussion).

The existence of the $L\beta_{2,15}$ doublet accompanied by a satellite line is supported by the qualitative data obtained by means of the high resolution spectrometer equipped with the quartz monochromator. As shown in Fig.12, a shoulder can be observed on the low wavelength side of the major peak. The separation distance between the peak maximum and the shoulder, ranges from $\simeq$ 0.0001 nm for Nd and $\simeq$ 0.00015 nm for Ho (Fig 12 a,b). These values are in good agreement with the calculated $L\beta_2 - L\beta_{15}$ separation distance. In addition, the spectra in Fig.12b clearly showed the existence of the $L\beta_{14}$ peak which was only detected as a result of the $L\beta_2$ peak deconvolution of the spectra obtained by means of the LiF monochromator.

Lγ lines and satellites : High resolution Lγ X-ray peaks obtained by means of the quartz monochromator (Johansson mounting) are shown in Fig.13 for Nd and Ho. The peaks exhibited a tail occurring on the long wavelength side of the $L\gamma_1$ diagram lines. A similar tailing effect was also in observed the digitally recorded data obtained using the LiF monochromator (Johann mounting) as shown in Fig.14.

The $L\gamma_1$ peaks were solved as a doublet assuming that each single peak had the same width. The instrumental correction factor was omitted for the $L\gamma_1$ peaks of La, Pr and Nd oxide crystals and was added into the fitting procedure of experimental data for the analyzed Sm, Eu, Gd, Dy, Ho, Er and Yb crystals.

For elements with an atomic number ranging from 57 (La) to 66 (Dy), calculations showed that the $L\gamma_1$ emission consists of two peaks, as illustrated in Fig.14 for the case of Nd. The peak of higher intensity

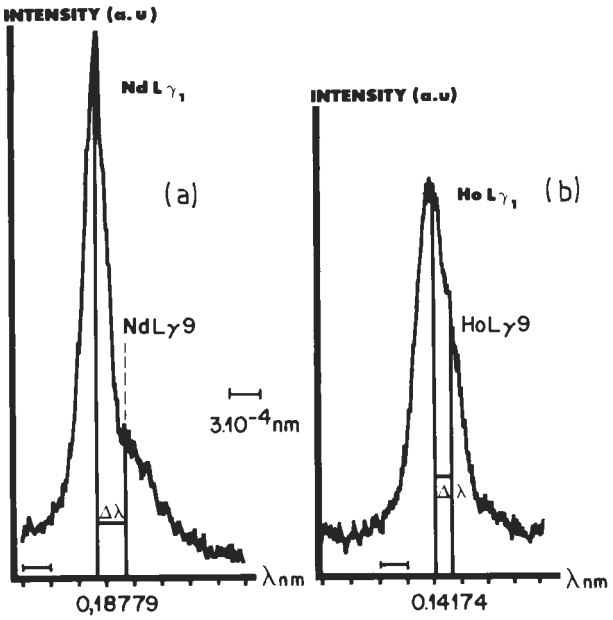

Figure 13. (a) $L\gamma_1$ diagram line and $L\gamma_9$ non-diagram line for Nd, and (b) Ho, shown by means of the quartz monochromator.

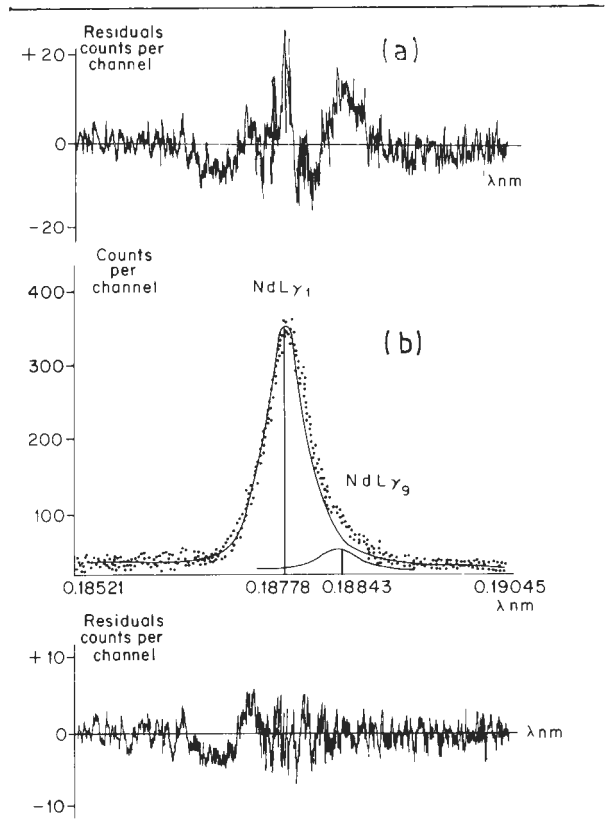

Figure 14. Results of fits and residuals to the Nd $L\gamma_1$ peak analyzed by means of the LiF monochromator using (a) a single component and (b) two components by means of pseudo-Voigt fitting functions.

corresponds to the $L\gamma_1$ diagram line (L_{II} - N_{IV} transition) and is accompanied by a weaker peak occurring on the long wavelength side of the $L\gamma_1$ peak. This weak peak is a satellite non-diagram line we labelled $L\gamma_9$ (see chapter Discussion). As shown in Fig.15a the intensity of both the $L\gamma_1$ diagram line and $L\gamma_9$ satellite varies linearly with the wavelength. The wavelength separation distance : $\Delta\lambda = \lambda(L\gamma_9) - \lambda(L\gamma_1)$ also varied linearly with wavelength of the characteristic peak as illustrated in Fig.15b.

For elements with atomic number greater than 66 (Dy), the fitting procedure did not reveal evidence for the existence of the satellite peak. This may result from the distance between the two lines being to small to be resolved if the positions and intensities of both peaks are kept as variables in the analytical procedure. In addition, the satellite peak may be partly hidden by the Gaussian correcting the instrumental spectral distortion. Thus, in order to verify that the $L\gamma_1$ emission for lanthanide elements with Z greater than 66 also consists of a doublet, only the peak heights of the two lines were used as variables in the fitting procedure. The wavelength of the assumed $L\gamma_9$ satellite was thus calculated by linear extrapolation from data obtained for the case of analyzed elements with $Z \leq 66$. The calculated peak heights derived from the fit were found to be in good agreement with the peak heights obtained by extrapolation (Fig.15a) of the linear variation existing for the $L\gamma_1$ and $L\gamma_9$ emissions of lanthanide elements with atomic numbers less than 66.

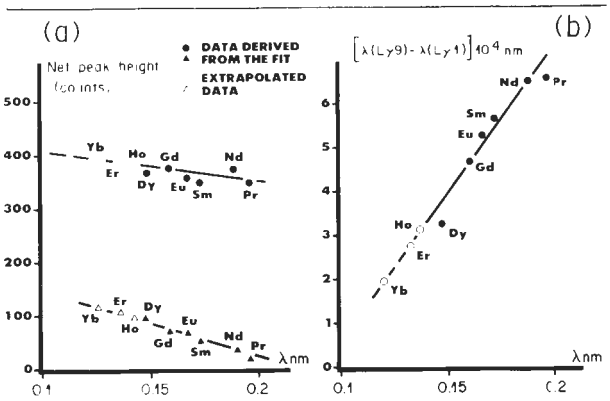

Figure 15. (a) Peak height variation of the $L\gamma_1$ (O's) and $L\gamma_9$ (Δ's) peaks, and (b) wavelength separation distance, $L\gamma_9$ - $L\gamma_1$, as functions of wavelength.

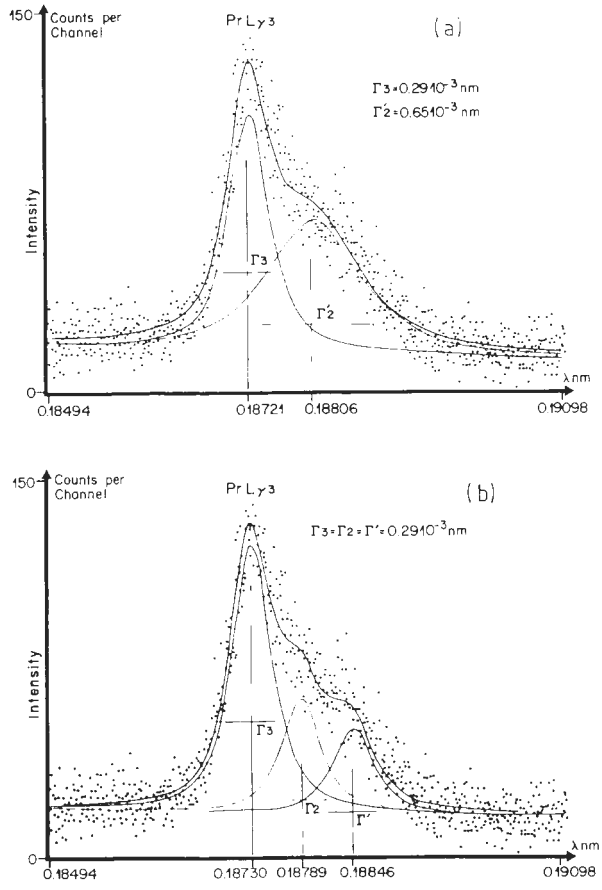

Figure 16. Data processing of the Pr ($L\gamma_2$ - $L\gamma_3$) doublet and Pr $L\gamma_{10}$ non-diagram line recorded by means of the LiF monochromator.
a) Least-square fitting procedure by means of two components.
b) Least-square fitting procedure by means of three components.

The $L\gamma_2$ and $L\gamma_3$ emission lines of light lanthanide elements consist of two partly resolved peaks as shown in Fig.16a for the case of Pr. Increasing the atomic number of the lanthanide, the $L\gamma_2$ - $L\gamma_3$ feature appears as a single broad peak. The spectra were processed as a doublet, with the peak position, peak width and peak amplitude of both components being kept as variables in the fitting procedure. Neither the position nor the width of the higher wavelength peak corresponded to the characteristics of the $L\gamma_2$ peak of the analyzed element. However, the calculated position of the lower wavelength intense peak corresponded exactly to that of the $L\gamma_3$ emission. In addition, the calculated width was in good agreement with the predicted value derived from the calibration curve. These parameters of the $L\gamma_3$ peak shape were kept constant and a third component was added to the fitting procedure. The HWHM values of the three peaks were assumed to be equal and the peak positions and peak heights were used as variables. The results in Fig.16b show the decomposition of the $L\gamma_2$; $L\gamma_3$ structure as a triplet for the case of Pr. The calculated position and width of the $L\gamma_3$ peak was unchanged with respect to data derived from the previous calculations. The calculated positions of the intermediate peaks exactly match the theoretical wavelength of the $L\gamma_2$ emission peak while the third peak, of the highest wavelength, is a non-diagram line we named $L\gamma_{10}$ (see Chapter Discussion). Similar data were obtained for the case of La, Nd and Sm. As shown in Fig.17a, the amplitude of the three peaks, $L\gamma_3$, $L\gamma_2$ and $L\gamma_{10}$ decreased linearly when the analyzed wavelength increased. As illustrated in Fig.17b the wavelength separations $L\gamma_{10}$ - $L\gamma_2$ and $L\gamma_{10}$ - $L\gamma_3$ increased linearly when the analyzed wavelength increased. For elements with atomic numbers greater than 62 (Sm) the $L\gamma_2$ and $L\gamma_3$ emission peaks are strongly distorted by the instrumental factor. Thus, each of the three peaks for these elements should be corrected for spectral distortion. The increasing number of variables in the fitting procedure will not lead to a unique solution. In addition, the

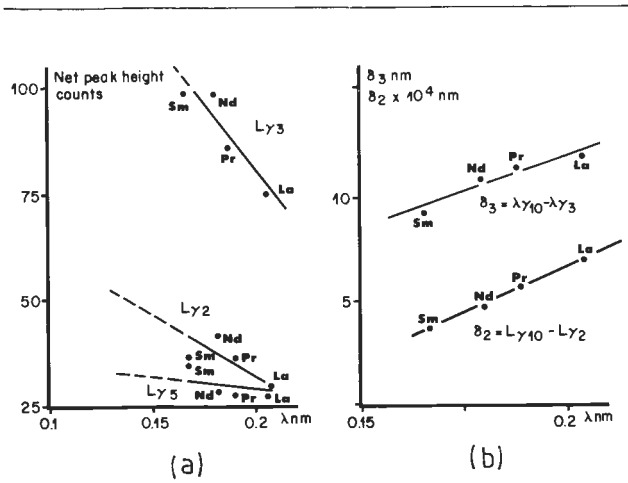

Figure 17. (a) Peak amplitude variations of the $L\gamma_2$, $L\gamma_3$ diagram lines and $L\gamma_{10}$ non-diagram line and (b) wavelength separation distances $L\gamma_{10}$ -$L\gamma_2$ and $L\gamma_{10}$ - $L\gamma_3$, as functions of the analyzed wavelength for the cases of La, Pr, Nd and Sm.

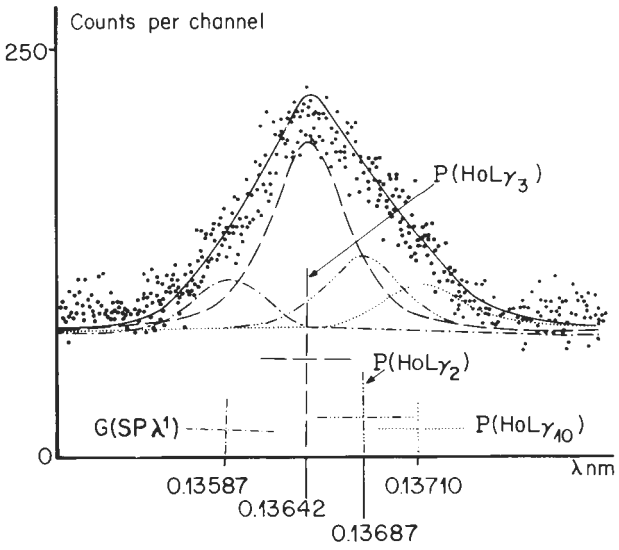

Figure 18. Ho $L\gamma_2$, $L\gamma_3$, $L\gamma_5$ line profile calculation based on HWHM and peak height values derived from linear extrapolation shown in figure 17 and accounting for spectral distortions resulting from the monochromator mounting.

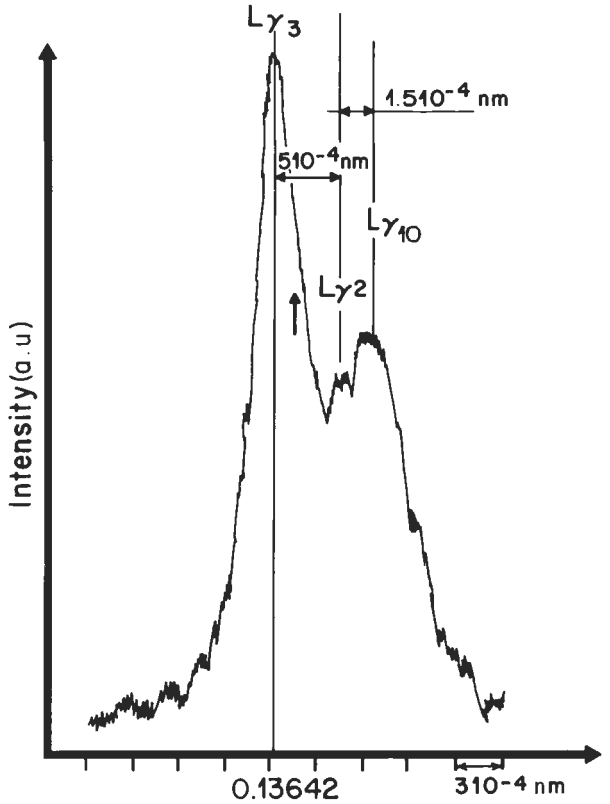

Figure 19. Fine structure of the Ho $L\gamma_2$ - $L\gamma_3$ diagram lines and non-diagram lines shown by the use of the quartz monochromator.

low intensity measured in the $L\gamma_2$ - $L\gamma_3$ emissions did not lead to a sufficient statistical precision to facilitate an accurate peak deconvolution.

For the lanthanide elements with high atomic numbers we simply calculated synthetic spectra by using peak width, peak intensity and peak position derived from linear extrapolation of the data describing the $L\gamma_3$, $L\gamma_2$, $L\gamma_{10}$ of the light lanthanide elements. As shown in Fig. 18 for the case of Ho, the $L\gamma_2$ - $L\gamma_3$ - $L\gamma_{10}$ features on the synthetic calculated spectra provided a satisfactory description of the experimental data. These calculations are also supported by the experimental spectra obtained by means of the high resolution quartz monochromator as illustrated in Fig.19 for the case of Ho. However the spectra obtained with the quartz monochromator suggest that the $L\gamma_{10}$ line consists of several lines which are not resolved in the spectra obtained by means of the LiF monochromator. The consequence of the different monochromator mounting is illustrated by comparing Fig.18 and Fig.19. The marked shoulder occurring on the low wavelength side of the Ho $L\gamma_3$ peak in Fig.18 (Johann mounting of the LIF monochromator) is not observed in Fig.19 (Johansson mounting of the quartz monochromator).

The wavelength separation distances $L\gamma_{10}$ - $L\gamma_3$ and $L\gamma_{10}$ - $L\gamma_2$ measured in the spectra of Fig.19 were $\simeq$ 0.006 nm and $\simeq$ 0.0015 nm respectively. These direct measurements from graphs are very consistent with those derived from the linear variation of the peak separation vs wavelength drawn for the light lanthanide elements (Fig.17b). For the case of Ho, the extrapolated wavelength separation distances were $L\gamma_{10}$ - $L\gamma_3$ = 0.0068 nm and $L\gamma_{10}$ - $L\gamma_2$ = 0.00018 nm respectively.

The consistency of the data obtained by means of both monochromators supports the existence of a satellite line accompanying the $L\gamma_3$ -$L\gamma_2$ emissions which were not resolved for the case of high atomic number lanthanide elements analyzed by the use of the LiF monochromator. The consistency of measured and extrapolated peak separations also strongly supports the observed linear relationship between the wavelengths of the satellite line and the diagram $L\gamma_3$ and $L\gamma_2$ emission peak positions.

Discussion

L X-ray peaks of the lanthanide elements were processed using a pseudo-Voigt function to distinguish doublets and satellite peaks from X-ray data derived by means of the LiF monochromator. All peaks occurring at wavelengths less than ≈ 0.17 nm exhibited a shoulder on their low wavelength side as a result of the monochromator characteristics. This deviation from symmetry was corrected by adding a Gaussian distribution to the pseudo-Voigt function describing the characteristic emission line. After spectral distortion resulting from instrumental factors was corrected, the variation of the peak-width as a function of wavelength was found to be dependent on the analyzed emission. As an example, the widths of $L\beta_3$, $L\beta_4$ and $L\gamma_1$ X-ray lines were found to be greater than those of $L\alpha_1$, $L\alpha_2$ and $L\beta_1$ lines of equivalent wavelength. In general, peak width decreases when increasing wavelength for a given peak. The Ll peak width, however increases with increasing wavelength. This situation results from the difference in the natural widths of the analyzed lines. The broadening of the $L\beta_3$ lines with respect to the width of an $L\alpha_1$ peak of equivalent wavelength results only from the difference in their natural widths. The effective calculated HWHM, derived from the fitting procedure with equation [12] is a sufficient approximation to generate synthetic L X-ray spectra which are used to determine the relative intensities of peaks. However, the use of an effective width is no longer sufficient once the analytical model is used to resolve a complex peak into the sum of several lines. For this purpose the width must be used as a fixed, predetermined parameter derived from the instrumental resolution of the monochromator Γi, and the natural width 2γ, of the analyzed emission. The importance of the natural width of an X-ray peak has been illustrated for the case of the $L\beta_3$ X-ray emission of the lanthanide elements.

The natural width of the $L\beta_3$ emission line is about twice that of the $L\alpha_1$ emission (21),(22). Neglecting this difference leads to the description of the $L\beta_3$ peaks of a lanthanide element as a doublet, each component having a width equal to that of an $L\alpha$ peak of equivalent wavelength. Taking the natural width into account resulted in describing the $L\beta_3$ peak as a single peak, consistent with the results from Sakellaridis (19).

A complex fine structure has also been shown to exist for the case of the $L\beta_4$ (L_I - M_{II}) emission (19). The low intensity of the $L\beta_4$ peaks, obtained with the LiF monochromator did not lead to a sufficient statistical precision to accurately process the $L\beta_4$ peaks, which were treated as single peaks. In the present study, non-diagram lines associated with the $L\beta_{2,15}$, $L\gamma_1$ and $L\gamma_{2,3}$ peaks have been analyzed. The existence of the satellite lines was observed in spectra obtained by the use of the high resolution quartz monochromator. Spectra deconvolution was only applied for peaks occurring within a wavelength domain in which the instrumental spectral distortion remained moderate. For the heavy lanthanide elements the characteristics of the satellite lines were obtained by linear extrapolation of peak separation distances and peak amplitudes calculated from experimental data obtained for light lanthanide elements. For consistency with data available in the literature, the measured wavelength distances between the major peak and its satellite were converted to energy units (eV).

Studying the L X-ray emission for Eu(63), Gd(64), Tb(65), Ho(67) and Tm(69), Sakellaridis (19) showed the existence of fine structures lying on the low energy side of the $L\beta_4$, $L\beta_2$, $L\gamma_1$ and $L\gamma_2$ peaks. He showed that the $L\beta_{2,15}$ doublet is accompanied by multiple weak peaks. In our study, the $L\beta_{2,15}$ doublet was partly resolved by the use of the quartz monochromator but was not resolved when using the LiF monochromator. By comparing the energy separation distances obtained by Sakellaridis (19) and our experimental data, we resolved a single satellite peak that is consistent (Table 2) with the strongest satellite line labelled as $L\beta_{14}$ in the Sakellaridis work (19)(see Fig. 12).

Fitting experimental L X-ray spectra of lanthanide elements and their oxide crystals using the sum of two Lorentzian shaped lines, Salem and Scott (23) showed the existence of a weak satellite line on the low energy side of the $L\beta_{2,15}$ characteristic line. The energy separation, ΔE, between the peak and its satellite are reported in Table 2. Salem and Scott (23) also showed that the ΔE values for lanthanide elements are lower by about 2eV than the energy separation for lanthanide oxide crystals. Results in Table 2 indicate, that, for oxides, our experimental energy separation distances are consistent with the data reported by Salem and Scott (23). For the cases of La and Pr, the amplitude of the

satellite line was too small to be accurately measured. The same conclusion was reached by Salem and Scott (23).

Table 2. Energy separation distance in eV between the $L\beta_{2,15}$ line and the $L\beta_{14}$ non-diagram line for lanthanide elements in lanthanide oxide crystals.

Z	This Study	Sakellaridis [19]	Salem and Scott [23]
La	nd (33.1Δ)		nd
Pr	nd (30.37Δ)		nd
Nd	23*		25.2
Sm	26*		28.0
Eu	24*	25.7	25.8
Gd	29.0* 23.5Δ	27.0	25.1
Tb	20.0Δ	26.8	22.4
Dy	17.0*		16.7
Ho	15.0*	18.0	14.6
Er	12.5Δ		14.4
Tm	10.5Δ		10.9
Yb	nd (6.5Δ)		nd

* calculated nd : not detected
Δ extrapolated

The characteristics of the satellite line we observed on the low energy side of the $L\gamma_1$ peak are also consistent with the data reported by Sakellaridis (19) and Salem and Scott (23) and calculated by Srivastava et al. (29). As for the case of the $L\beta_2$-β_{14} feature, the fitting procedure used in the present study and by Salem and Scott (23) allowed us to identify a single satellite line associated with the $L\gamma_1$ emission, while Sakellaridis (19) showed that a very fine complex structure accompanied the main $L\gamma_1$ peak. As shown in Table 3, the comparison of energy separation distances between the $L\gamma_1$ line and its satellite leads to the conclusion that the non-diagram line we detected corresponds to the satellite labelled as $L\gamma_9$ in the Sakellaridis work (19).

Sakellaridis (19) showed that the $L\gamma_3$-$L\gamma_2$ feature is very complex and contains very weak peaks occurring on the low and high energy sides of the $L\gamma_2$ peak simultaneously. Some of these small features were shown on spectra obtained by means of the quartz monochromator (see Fig. 19). However, when using the LiF monochromator, none of the weak peaks occurring between the $L\gamma_3$ and $L\gamma_2$ emission line were detected. The non-diagram lines on the low energy side of the $L\gamma_2$ peak were solved as a single peak in the fitting procedure. The measured separation distance between the $L\gamma_2$ peaks and satellites are consistent with the separation distances reported by Sakellaridis (19) between the $L\gamma_{10}$ non-diagram lines and $L\gamma_2$ peaks for Eu(63), Gd(64), Tb(65) and Ho(67).

Also consistent with the results from Sakellaridis (19), the $L\gamma_{10}$-$L\gamma_2$ energy separation distances were found to be slightly less than for those of the $L\beta_{14}$-$L\beta_2$ and $L\gamma_9$-$L\gamma_1$ peaks.

Several theories have been proposed to account for the existence of non-diagram lines (8). Particular attention has been paid to the $k\beta'$ low energy satellite associated with the $K\beta_{1,3}$ emission resulting from transitions involving the partially filled 3d shells of transition elements and their oxides.

Table 3. Energy separation distances in eV between the $L\gamma_1$ line and the $L\gamma_9$ non-diagram line for lanthanide elements in lanthanide oxide crystals.

Z	This Study*	Sakellaridis (19)	Salem Scott (23)	Srivastava et al.** (29)
La	22.3		nd	
Pr	22.6		24.3	23.53
Nd	22.7		20.1	23.14
Sm	22.0		21.5	21.43
Eu	21.7	24.1	21.8	20.48
Gd	21.5	25.6	21.5	21.01
Tb	21.0	26.4	19.6	
Dy	19.8		17.4	19.55
Ho	18.9	15.8	17.8	
Er	17.1		18.9	16.40
Yb	15.3		nd	

* Average ΔE values derived from the linear regression expressing the wavelength separation distance as a function of wavelength.

** Calculated data based on the plasmon oscillation theory (see text).

nd : not detected

According to Tsutsumi and Nakamori (30) and Tsutsumi et al.(31) the $K\beta'$ satellite originates from the interaction between the electrons in the incomplete 3d shell and the hole in the incomplete 3p shell resulting from the $K\beta_{1,3}$ radiative transition. A similar theory has been proposed by Salem et al.(20) in which the exchange interaction splits both 3p and 3d electron levels, causing some 3p electrons to move to lower energy levels. Transitions from these levels appearing as emission bands on the low energy side of the $K\beta_{1,3}$ peak.

Low energy satellites can also be explained as the result of single-photon two-electron rearrangement transitions as discussed by Jamison et al.(11) for the case of K X-rays.

Two types of single-photon two-electron rearrangement transitions are the radiative electron rearrangement (RER) and the radiative Auger effect (RAE), respectively. In a RER process a K X-ray photon is emitted coincident with two 2s electrons undergoing rearrangement. One of the 2s electrons fills the K shell vacancy, while the other is promoted to the 2p subshell. The lowest energy RER satellite is the transition from states with one 1s and one 2p vacancy. The RAE process results from a de-excitation of a K vacancy, similar to an Auger process with simultaneous emission of a bound electron and an X-ray photon. The $K\beta'$ satellite of the $K\beta_{1,3}$ lines of transition metals has been interpreted in terms of the K-MM radiative Auger effect by Servomaa and Keski-Rahkonen (24) and Keski-Rahkonen and Ahopelto (12). Campbell et al (4) added the existence of RAE while studying the $K\alpha/K\beta$ ratios of X-ray spectra induced by proton bombardment of atoms in the $20 < Z < 40$ region. Recently, Srivastava et al. (28) proposed an alternative explanation for the $K\beta'$ satellite based on the plasmon oscillation in solids.

According to the plasmon oscillation theory, during the X-ray emission process, the transition valence electron excites a plasmon in the valence band. The transition energy of the $K\beta_{1,3}$ line will thus be shared between the plasmon and the emitting photon, which will be deprived of an energy equal to the plasmon energy, $\hbar\omega p$ which is used to excite the plasmon.

These theories were extended to the case of the L X-ray spectra of the lanthanide elements. The $L\beta_2$, $L\beta_4$, $L\gamma_1$ and $L\gamma_2$ emissions exhibiting low energy satellites are associated with transitions involving the partially filled 4f shell. According to Sakellaridis (19) the fine multiple structures result from the splitting of levels. In addition, the electron spin may have a role in the satellite production since the $L\gamma_2$ (L_I - N_{II}) and $L\beta_4$ (L_I - M_{II}) are split while the $L\gamma_3$ (L_I - N_{II}) and $L\beta_3$ (L_I - M_{III}) are not. This conclusion was used in our $L\beta_3$ data processing and illustrates the importance of the natural width of X-ray lines in WDS peak deconvolution. Similarly, Salem and Scott (23) explained the existence of the low energy satellite accompanying the $L\gamma_1$ emission as a result of the exchange interaction between the 4f and 4d electrons, which splits both levels ; the transitions taking place between the split levels giving rise to the non-diagram lines.

The theory based on plasmon oscillation was also extended by Srivastava et al.(29) from the case of the $K\beta'$ satellite of transition elements to that of the satellite lines accompanying the $L\gamma_1$ emission of lanthanide elements. Srivastava (27) calculated the plasmon energy, $\hbar\omega_p$, according to the relationship :

$$\hbar\omega_p = 28.8 \left(\frac{Z'\sigma}{W}\right)^{1/2} \qquad [24]$$

where $\hbar\omega_p$ is given in eV, Z' is the effective number of free electrons taking part in plasmon oscillations, σ is the specific gravity of the material and W is the molecular weight. Equation [24], valid for the free electron model, was also applied by Srivastava et al. (29) to the case of insulators such as lanthanide elements and their oxides. As shown in Table 3, the $\hbar\omega_p$ values calculated according to equation [24] by Srivastava et al. are in fairly good agreement with the energy separations between the $L\gamma_1$ line and its satellite observed by Salem and Scott (23) and those obtained in this study.

Owing to spectral distortions resulting from instrumental factors, the wavelength separation distance $\Delta\lambda$ between the $L\gamma_1$ emission and its $L\gamma_9$ satellite for the heavy lanthanide elements had to be derived from linear extrapolation (Fig. 15b) of experimental data for light lanthanide elements.

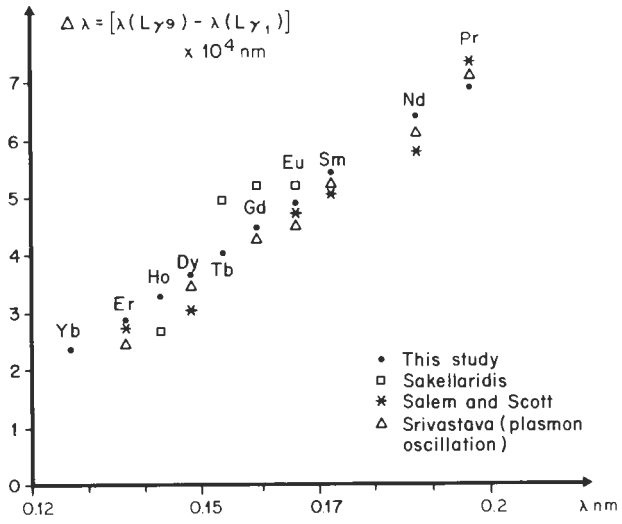

Figure 20. Comparison of wavelength separation distances $L\gamma_9 - L\gamma_1$ as a function of wavelength derived from the experimental measurements (this study) and from the energy separation distances observed by Salem and Scott [23] and calculated by the plasma oscillation theory according to Srivastava et al. [29].

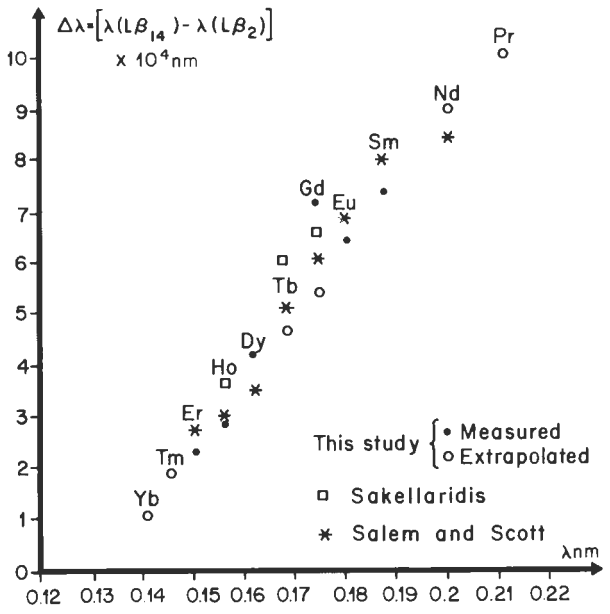

Figure 21. As in Fig. 19 for the case of the $L\beta_{14} - L\beta_2$ wavelength separation distance vs wavelength.

The measured energy separations as a function of the atomic number of the lanthanide elements reported by Salem and Scott (23) and by Sakellaridis (19) were compared to our experimental data. According to these authors (see Table 3) the energy separation increased linearly as a function of the atomic number. Expressing the separation in terms of wavelength and using the wavelength of the $L\gamma_1$ line as a variable rather than the atomic number, a linear relationship of the wavelength separation $L\gamma_9$-$L\gamma_1$ vs wavelength was observed (Fig. 20) both for the experimental data derived from the Salem and Scott work (23) and from the present study. These variations are in excellent agreement with those obtained by identifying the measured wavelength separation $L\gamma_9$-$L\gamma_1$ with the wavelength separation derived from the plasmon $\hbar\omega_p$ values according to Srivastava, et al. (29).

Similar conclusions were drawn for the case of the $L\beta_{14} - L\beta_2$ energy separation distance. According to Sakellaridis (19) the separation increased linearly as the atomic number of the analyzed element increased up to 65 (Tb) and then abruptly decreased. As shown in Fig. 21, the $L\beta_{14}$-$L\beta_2$ separation distance plotted in terms of wavelength distance showed a linear variation as a function of the wavelength. A different relationship between energy distance and atomic number was observed for $L\gamma_{10} - L\gamma_2$ by Sakellaridis (19). According to this author (19) the $L\gamma_{10} - L\gamma_2$ energy difference slowly decreased up to the atomic number Z = 65 (Tb) and then abruptly decreased.

This difference in the sign of the variation of wavelength vs $L\gamma_{10} - L\gamma_2$ distance with respect to that of the $L\gamma_9 - L\gamma_1$ distance within the atomic number domain $57 < Z < 65$ was not observed in the present study.

We compared these results with the ratio of the radiative transition probability $I(L\gamma_9)/I(L\gamma_1)$ as a function of the atomic number of the lanthanide elements as published by Salem and Scott (23) and Srivastava et al.(29), respectively. Salem and Scott (23) showed that the ratio between the $L\gamma_9$ and $L\gamma_1$ line intensities increased with increasing the atomic number of the element increased up to Z = 64 (Gd), and then decreased. The apparent change in slope at Gd may be due to the fact that Gd is the only lanthanide element having a $4f^7 5d6s$ ground-state configuration rather than the usual $4f^N 6s^2$.

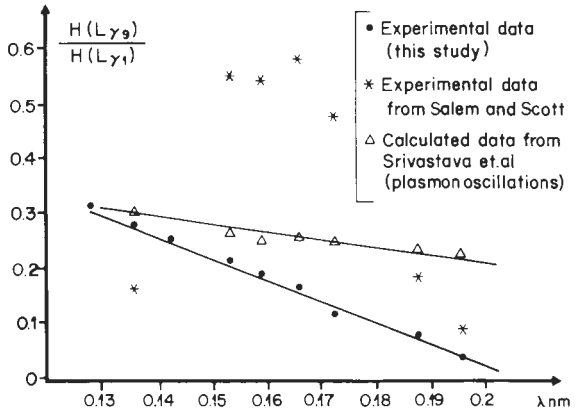

Figure 22. Relative intensity of the $L\gamma_9$ non-diagram line with respect to that of the $L\gamma_1$ diagram line vs wavelength according to various sources of observed and calculated data.

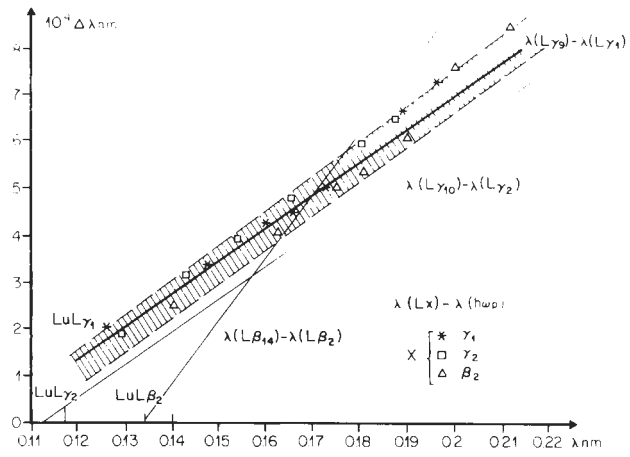

Figure 23. Comparison between observed ($L\gamma_9$ - $L\gamma_1$), ($L\gamma_{10}$ - $L\gamma_2$), and ($L\beta_{14}$ - $L\beta_2$) distances and the separation distances calculated as the difference in the characteristic wavelength of the diagram line and that associated with the volume plasmon.

A linear relationship between $L\gamma_1$ vs wavelength and the $L\gamma_1$ and $L\gamma_9$ relative transition probabilities is also supported by the calculated values based on the plasmon theory as proposed by Srivastava et al.(29). Although the slope is different, the intensity ratio between the $L\gamma_1$ and $L\gamma_9$ lines derived either from our experimental measurements or from the plasmon theory calculations exhibited a linear variation as a function of wavelength (Fig. 22).

The relative intensities observed by Salem and Scott (23) are in better agreement with the calculated values of Srivastava et al. (29) based on the plasmon theory, than those calculated by Salem and Scott (23). Salem and Scott (23) concluded that the 4d - 4f exchange theory is certainly present but cannot surely be the sole cause of the splitting of the 4d level.

In this study, the multiple satellite lines were not completely resolved, owing to the low energy resolution of the spectrometer used. The non-diagram lines, $L\beta_{14}$, $L\gamma_9$ and $L\gamma_{10}$ were solved as single peaks. In addition, the HWHM values of the satellite peaks were assumed to be equal to those of the parent diagram peaks, $L\beta_2$, $L\gamma_1$ and $L\gamma_2$, respectively.

These simplifications are supported by our objective, which aimed to provide an analytical description of complex X-ray spectra to be used in a least-squares fitting procedure. Furthermore, for calculations, the wavelength distances, $L\beta_{14}$-$L\beta_2$, $L\gamma_9$-$L\gamma_1$, $L\gamma_{10}$-$L\gamma_2$ were set equal to those based on the plasmon theory as shown in Fig. 23.

The width of the Ll peaks was found to increase as a function of wavelength (Fig. 5) and to be much greater than that of the other L X-ray peaks of the lanthanide elements. The Ll emission lines of the analyzed pure elements W, Pt and Au occur in a wavelength domain in which instrumental spectral distortions lead to inaccurate processing of low intensity Ll peaks. It was thus not possible to conclude that the positive correlation between width and wavelength of the Ll peaks is characteristic only of the lanthanide elements. In addition, only little data concerning the natural width of the Ll X-ray emission peaks are available in the literature (23). The change in the natural width of the Ll emission as a function of the atomic number is not sufficient to explain the variations observed in the effective widths as a function of wavelength (Fig. 5). The Ll peaks obtained by means of the quartz monochromator exhibited an apparent symmetrical shape, therefore the Ll X-ray lines were assumed to be single peaks and their effective widths derived from the fitting procedure were used to generate synthetic spectra.

While the pseudo-Voigt function and the associated Gaussian distribution which were used to correct for instrumental spectral distortion (equation [13]) were sufficient approximations to generate L X-ray emission spectra, they were not sufficient to satisfactorily describe the $K\alpha_1$-α_2 X-ray peaks of the transition elements analyzed with the same LiF monochromator.

For example, the $CrK\alpha_1$ and $CrK\alpha_2$ X-ray emissions (λ = 0.229 nm and λ = 0.2294 nm, respectively) are very close to that of the Nd $L\alpha_1$ X-ray peak (λ = 0.2371 nm). These K emissions lie in a wavelength region that is not affected by the spectral distortion resulting from the monochromator mounting. The $CrK\alpha_1$ and $CrK\alpha_2$ lines were not completely resolved. In the fitting procedure the peak positions were set at their theoretical values and the $CrK\alpha_1$ peak intensity was set at twice the $CrK\alpha_2$ peak intensity. Only the HWHM values were kept as variables. Using k = 0.35 to account for the Gaussian portion of the pseudo-Voigt fitting function did not lead to a satisfactory fit. The calculated HWHM values were found to be much less than those predicted from the calibration curve even accounting for the correction for the natural width of the lines. These observations remained valid for all analyzed $K\alpha$ lines of the elements with atomic numbers ranging from Z = 22 (Ti) to Z = 31 (Ga). However, the quality of the fit was slightly improved when the k value in equation [8] was increased from k = 0.6 to k = 1.0 as the atomic number of the analyzed element was increased. Thus, the proportion of the Gaussian contribution with respect to the Lorentzian distribution was found to differ for $K\alpha$ and $L\alpha$ lines occurring within the same wavelength region. This observation is consistent with the results reported by Huang and Lim (10).

Summary

The shape of $L\alpha$ X-ray peaks analyzed by means of LiF monochromator has been shown to be correctly described by a pseudo-Voigt function, i.e., a linear combination of a Gaussian distribution and a Lorentzian distribution having the same width and amplitude and centered at the same wavelength. For the monochromator used, the proportion of the Gaussian distribution was 0.35 and the Lorentzian distribution was 0.65. Spectral distortion has been shown to result from the monochromator mounting type ; the Johann mounting type results in a shoulder occurring on the low wavelength side of the X-ray peaks. The importance of these distortions depends on the wavelength of the analyzed X-ray peak and becomes negligible for wavelengths greater than $\approx$ 0.17 nm, i.e., for a Bragg angle greater than $\approx$ 35°.

The peak shape distortion for wavelengths less than $\approx$ 0.17 nm was corrected by adding a Gaussian distribution to the pseudo-Voigt function used to analytically describe the peak profile.

The model was applied to the study of complex L X-ray spectra (0.11 nm < λ < 0.27 nm) detected by a LiF monochromator (200 plane) that was set into the spectrometer with a Johann mounting.

After correcting raw data for possible spectral distortion resulting from the crystal mounting, the observed width of $L\alpha$ peaks exhibited a linear variation as a function of the analyzed wavelength. This linear relationship was used to determine the instrumental response function of the spectrometer.

It has been shown that the width calculated by quadrature addition of the intrinsic resolution and the natural width of the X-ray line emission leads to a sufficient approximation to the correct prediction of the width of any X-ray peak of an L X-ray emission analyzed by means of LiF monochromator. In addition, it has also been demonstrated that neglecting the natural width in the fitting procedure may lead to the detection of spurious peaks which can be assigned as satellite lines as demonstrated for the case of the $L\beta_3$ emission of the lanthanide elements. For these elements the $L\beta_2$, $L\gamma_1$ and $L\gamma_2$ were found to be accompanied by non-diagram (satellite) lines, $L\beta_{14}$, $L\gamma_9$ and $L\gamma_{10}$, respectively. These satellite lines occur on the long wavelength side of the characteristic peak. The observed wavelength separation distances, $L\beta_{14}$ -$L\beta_2$, $L\gamma_9$ - $L\gamma_1$ and $L\gamma_{10}$ -$L\gamma_2$ were consistent with data reported in the literature (19), (23); (29) and have been shown to vary linearly as a function of the wavelength of the $L\beta_2$, $L\gamma_1$ and $L\gamma_2$ diagram lines. The linear dependence of the $L\gamma_9$ - $L\gamma_1$ distances with respect to $L\gamma_1$ wavelength is also consistent with the distances calculated by Srivastava (29) based on the plasmon theory.

The linear correlations of wavelength with the relative probabilities of $L\beta_{14}/L\beta_2$, $L\gamma_9/L\gamma_1$ and $L\gamma_{10}/L\gamma_2$ are also consistent with the calculated data according to the plasmon

theory (29). The mechanism leading to the existence of non-diagram lines associated with the $L\beta_2$, $L\gamma_1$ and $L\gamma_2$ emission as observed in the present study is probably much more complex than that based on the plasmon oscillation theory proposed by Srivastava et al. (29) for the case of the $L\gamma_1$ emissions of lanthanide elements. However, from a practical point of view, identifying the energy separation between the $L\beta_2$, $L\gamma_1$ and $L\gamma_2$ lines and their satellites with the plasmon value led to a sufficient approximation for our purpose.

The simplified analytical model for describing L X-ray spectra provides an easy approach to generate synthetic spectra to be used either for the calculation of overlap coefficients to be applied to raw intensity measurements (peak height) or to process experimental data by means of least-squares fitting techniques in quantitative analysis based on WDS X-ray spectrometry by means of the EPMA.

References

[1] Anghelow BM, Wanklyn BM, (1986). Flux growth of lithium rare-earth tetraphosphates. J. of Materials Science Letters, 5, 1067-1069.

[2] Bonnelle C, Karnatak RC, (1971). Distribution des états 4 f dans les métaux et les oxydes de terres rares (Distribution of 4 f states in rare-earth elements and their oxides). Journal de Physique, Colloque C 4, 32, Supplément au n° 10, 230-235.

[3] Campbell JL, Perujo A, Millman BM, (1987). Analytic description of Si (Li) spectral line shapes due to monoenergetic photons. X-ray spectrometry, 16, 195-201.

[4] Campbell JL, Perujo A, Teesdale WJ, Millman BM, (1986). Kα, Kβ and radiative Auger photon intensities in K X-ray spectra from atoms in the $20 < Z < 40$ region. Physical Review A, 33, n° 4, 2410-2417.

[5] Coutures JP, Rifflet JC, Billard D, Coutures Ph, (1987). Contactless treatments of liquids in a large temperature range by an aerodynamic levitation device and laser heating ; Proc. 6th European Symposium on Material Sciences under Microgravity Conditions, 2-5 decembre 1986, Bordeaux, France, ESA Special Publication, Février 1987, 25 b, 427-430.

[6] Doyle BL, Chambers WF, Christensen TM, Hall JM, Pepper GH, (1979). Sine θ settings for X-ray spectrometers. Atomic Data and Nuclear Data Tables, 24, n° 5, 373-493.

[7] Drake DJ, Weill DF (1982). New rare earth element standards for electron microprobe. Chemical Geology, 10, 179-181.

[8] Edwards SJ (1970). A review of the theories of X-ray stalellite lines. Contemp. Phy., 11, n° 2, 195-200.

[9] Fiori CE, Myklebust RL, Gorlen K. (1981). Sequential Simplex : A procedure for resolving spectral interference in energy dispersive X-ray spectrometry. Energy Dispersive X-ray Spectrometry, KFJ Heinrich, DE Newbury, RL Myklebust and CE Fiori (eds), NBS Special Publication 604, 233-272.

[10] Huang TC, Lim G, (1986). Resolution of overlapping X-ray fluorescence peaks with the pseudo-Voigt function. Adv. X-ray Anal., 29, 461-468.

[11] Jamison KJA, Hall JM, Oltjen J., Woods CW, Kauffman RL, (1976). Single-photon two-electron rearrangement transitions. Physical Review A, 14, n° 3, 937-945.

[12] Keski-Rahkonen O, Ahopelto J, (1980). The $K \rightarrow M^2$ radiative Auger effect in transition metals : II. J. Phys. C : Solid St Phys., 13, 471-482.

[13] Labar JL, (1987). Effect of relative L-line intensity ratios on the accuracy of standardless X-ray microanalysis. X-ray Spectrometry, 16, 33-36.

[14] Lejus AM, Collongues R, (1980). Lanthanide oxides, structural anisotropy, physical and mechanical properties. Current Topics in Materials Science, 4, Kaldi E. (ed), North-Holland Publishing Company, 481-577.

[15] McCarthy JJ, Schamber FH, (1981). Least-squares fit with digital filter : a status report. Energy Dispersive X-ray Spectrometry, KFJ Heinrich, DE Newbury, RL Myklebust, CE Fiori (eds), NBS Special Publication 604, 273-296.

[16] Massiot D, (1985). Shape comparison of physical spectra : Application to Mossbauer spectra of silicate glasses. J. of Non-crystalline Solids, 69, 371-380.

[17] Phillips GW, Marlow KW, (1976). Automatic analysis of gamma-ray spectra from germanium detectors. Nuclear Instruments and Methods, 137, 525-536.

[18] Roeder PL, (1985). Electron microprobe analysis of minerals for rare-earth elements : use of calculated peak-overlap corrections. Canadian Mineralogist, 23, 263-271.

[19] Sakellaridis P, (1955). Multiplets caracteristiques des terres rares dans leurs spectres d'émission X. Le Journal de Physique et le Radium, 16, 422-427.

[20] Salem SI, Hockney GM, Lee PL, (1976). Splitting of the 3 p levels in the transition elements and their oxides. Physical Review A, 13, n° 1, 330-334.

[21] Salem SI, Lee PL, (1974). Widths of the L X-ray lines of the rare-earth elements. Physical Review A 10, n° 6, 2033-2036.

[22] Salem SI, Lee PL, (1979). In : CRC Handbook of Chemistry and Physics, RC Weast, MJ Astle (eds), CRC Press Inc., Boca Raton, FL. USA, E 207.

[23] Salem SI, Scott BL, (1974). Splitting of the 4 d 3/2 and 4 d 5/2 levels in rare-earth elements and their oxides. Physical Review A, 9, n° 2, 690-696.

[24] Servamaa A., Keski-Rahkonen O, (1975). K → M^2 radiative Auger effect in transition metals : I. J. Phys. C. : Solid State Phys., 8, 4124-4130.

[25] Smith DGW, Reed SJB, (1982). Rare-earth element determinations by energy-dispersive electron microprobe techniques, Inst. Phys. Conf. Ser., n° 61, Chapter 4, 159-162.

[26] Speer JA, Solberg TN, (1982). Rare-earth pyrosilicates (RE_2 Si_2 O_7) as potential electron microprobe standards. Microbeam Analysis, KFJ Heinrich, (ed), San Francisco Press, San Francisco, CA, USA, 445-446.

[27] Srivastava KS, (1980). Widths of conduction bands in metals. Journal of Electron Spectroscopy and Related Phenomena, 20, 319-322.

[28] Srivastava KS, Singh S., Srivastava AK, Nayal RS, Chaubey A., Gupta P, (1982). Electron-electron interaction in transition metal X-ray emission spectra. Physical Review A, 25, n° 5, 2838-2844.

[29] Srivastava KS, Srivastava AK, Husain KSM, Singh S, (1983). Electron-electron interaction in the X-ray emission spectra of rare-earth element and their oxides, Indian Journal of Pure and Applied Physics, 21, 256-257.

[30] Tsutsumi K, Nakamori HG, (1968). X-ray K emission spectra of chromium in various chromium compounds. J. Phys. Soc. Jpn., 25, n° 5, 1418-1423.

[31] Tsutsumi K, Nakamori H, Ichikawa K, (1976). X-ray Mn Kβ emission spectra of manganese oxides and manganates. Physical Review, B 13, n° 2, 929-933.

Discussions with Reviewers

J.L. Campbell : Please indicate how your conclusions will affect or assiste in particular types of analysis carried out by EPMA.

J. Back : How did you incorporate this information into an analytic package for analyzing REE-bearing minerals (e.g. monazite). I should be very interested in seeing the results obtained and how they compare with analyses obtained without these corrections.

Authors : Analytical description of the L X-ray spectra was first justified by the need in determining exact intensity ratios (branching ratios) in order to derive predetermined coefficients for peak overlap correction. Some lanthanide elements bearing oxide crystals being, difficult to obtain synthetic spectra were required for the calculation of some of the overlap correction coefficients. An example of the efficiency of the correction of raw data by means of preditermined coefficients is illustrated in Table 4 for the case of a monazite specimen.

Table 4 : Analysis of a monazite specimen by means of WDS X-ray spectrometry.

Z	K ratio	Calculated concentrations	
		raw data	after overlap correction
F	0.0014	0.0052	0.0061
Fe	0.0009	0.0009	0.0009
P	0.0773	0.1334	0.1331
Co	0.0085	0.0088	0.0090
La	0.1150	0.1309	0.1331
Th	0.0473	0.0630	0.0630
Ce	0.2323	0.2212	0.2276
Cl	0.0005	0.0007	0.0007
Pr	0.0464	0.0515	0.0442
Nd	0.0904	0.1011	0.0975
Sm	0.0188	0.0216	0.0143
Eu	0.0047	0.0056	0.0000
Gd	0.0246	0.0301	0.0000
Dy	0.0024	0.0030	0.0031
O*		0.2871	0.2716
sum		1.0642	0.9970

* by stoichiometry

A relative difference of ≃ 15 % is observed between the raw and corrected data for Pr resulting from the contribution of the La $L\beta_1$ peak to the Pr $L\alpha$ peak. The relative difference is increased up to 50 % for the case of Sm resulting from the overlap between $CeL\beta_2$ and $SmL\alpha_1$ peaks.

Peak interferences between the La $L\gamma_3$ and Ce $L\alpha_1$ peaks with the Gd $L\gamma_1$ emission leads to a spurious Gd concentration equal to 3 %. A similar spurious Eu concentration (0.3 %) results from the Pr $L\beta_2$ and Nd $L\gamma_3$ overlapping the Eu $L\alpha_1$ peak. Correction by means of predetermined coefficients can only be applied after accurate measurements have been obtained for both the peak and background intensities. Consequently, for minor and trace elements a least-squares fitting technique would be prefered to the usual peak height measurements.

Analytical description of X-ray spectra can be used as reference data in the fitting procedure. In order to improve the quality of the fit and to avoid spurious peaks it is necessary to take into account all features leading to departure from symmetry of X-ray peaks. For this reason correction for instrumental factors and non-diagram lines were added to the fitting function.

D. Newbury : How do the results vary when different LiF crystals are employed ? Does the peak shape show any unexpected variation from one crystal to the next as a result of the details of the crystal mosaic structure ?

I. Steele : With regard to content, the authors should consider the possible effects of using their derived peak fits and relations of shape with wavelength with other spectrometers which may not be aligned well or have analyzing crystals of different perfection. My worry is that someone might attempt to use their derived peak fit data on another system which has inherently different instrumental parameters. This is not a shortcoming of the study but rather a warning that all instruments, crystals, etc. do not have the same resolution, peak symmetry etc.

Authors : The crystal mosaic structure will affect both the efficiency and the energy resolution of the monochromator. However, the intensity of any X-ray emission peak relative to that of the intense Kα, Lα or Mα peak will remain independent of the efficiency of the monochromator while the energy resolution will vary from the LiF monochromator used to another.

The EPMA used was equipped with two LiF crystals. A shown in Fig. 24 for both

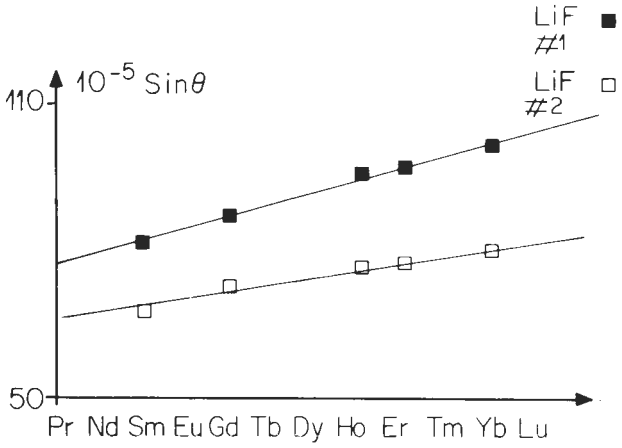

Figure 24. Wavelength resolution (10^5 sin θ) for two LiF monochromators as a function of the atomic number of some lanthanide elements.

crystals, the observed energy resolution for Lα peaks of some lanthanide elements exhibited a linear variation as a function of the atomic number of the analyzed elements. However, the slope of the linear relationship was different for each LiF monochromator used. This difference may result from the difference in the active area of each crystal leading to a more or less pronounced assymmetry of peaks. One of the monochromator (LiF ≠ 1) had its surface reduced by lead strips while the total area of the second monochromator (LiF ≠ 2) was used.

All equations obtained by the use of the first LiF monochromator remain valid by replacing the HWHM values by data derived from the calibration curve for the second LiF monochromator. Based on the linear relationship expressing the resolution vs wavelengths two measurements are sufficient to obtain the calibration curve for of another LiF monochromator.

S.J.B. Reed : How do the authors interpret the observation that the pseudo-Voigt function used for the L lines does not satifactorily fit K lines of the same wavelength ?

Authors : For the case of Kα peaks, the best quality of the fit was obtained by using a higher proportion of the Gaussian within the pseudo-Voigt function than that used for the description of Lα peaks of equivalent wavelengths. This observation is consistent with data reported by Salem and Scott (23) and by Salem et al. (20). In addition, we recently verified that the Lα peaks of transition elements (TAP crystal) were correctly described by the sum of two Lorentzian distributions.

A more pronounced Gaussian shape for Kα peaks than for Lα peaks is supported by the lower natural widths (Lorentzian distribution) for Kα lines with respect to Lα lines of equivalent energy. We assumed that the differences observed between K and L peaks resulted from the use of the pseudo-Voigt function which only takes into account the effective HWHM values. However, quadrature addition of the instrumental response function and natural widths of the analyzed Kα peaks was not sufficient to correctly described Kα peaks. New calculations will be performed using natural width values published by Scofield (Atomic Data and Nuclear Data Tables, (1974), 14, 121). In addition the complete convolution product given by equation [1] will be solved using the pseudo-Voigt function as the instrumental response function.

However the observed shape differences between Kα and Lα peaks more probably resulted from a marked asymmetry of Kα peaks which was not corrected. In the present study only departure from symmetry (tail on the low wavelength side of peaks) resulting from the monochromator mounting was corrected. Asymmetry of Kα peaks also exists as reported by LG Parratt (1959) and illustrated in Fig. 25 reprinted from the paper "Electronic band structure of solids by X-ray spectroscopy" (LG Parratt, 1959, Reviews of Modern Physics, 31, n° 3, 616-645). According to this author the excess width on the low-energy side (long wavelength side) is essentially attributable to transitions between excitation states of the valence-electron configuration type. Parratt also showed that the apparent excess of width for Kα peaks for atomic numbers through the range Z - 16 to Z = 42 is closely related to the asymmetry of peaks. The lines from transition $K \rightarrow L_{III}$ are presumed to be symmetrical and to be obtained by subtracting the mirror image of the high-energy side of the maximum position of the corrected observed curve from the low-energy side (Fig. 25).

It is this symmetrical component which should be compared to the calculated width obtained by quadrature addition of the instrumental width and natural width. Correction for asymmetry on the low-energy side of Kα peaks will be added to the fitting function.

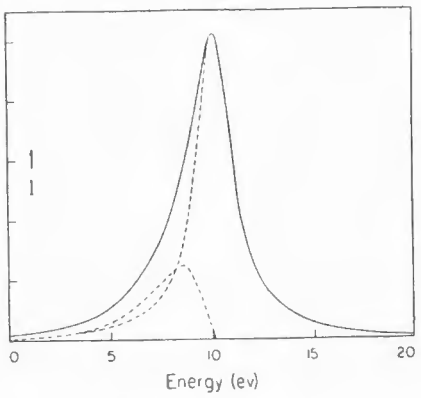

Figure 25. Asymmetric Kα peak according to LG Parrat (Reviews of Modern Physics, 1959, 31, n° 3, 616-645.